UNIVERSITY OF LATVIA
INSTITUTE OF CHEMICAL PHYSICS

Boris Polyakov

Structure, mechanical and electroconductive properties of nanomaterials

Doctoral thesis in physics

Riga 2006

ABSTRACT

In recent time nanoscale materials such as carbon nanotubes, metal and semiconducting nanowires, nanoparticles, fullerenes, nanodots were thoroughly investigated in many aspects of their properties. However, the technology of integration of many individual nanoobjects into functional devices is in early development stage. Nanotechnology proposes utilization of nanowires and it self-assembled architectures for electrical addressing of individual nanoobjects.

In this PhD work Ge nanowire ordered arrays synthesized inside porous anodized aluminum oxide (AAO) and DNA molecule architectures are investigated as well as their application possibilities.

Ge nanowires inside AAO membranes are found to be well ordered. The packing density of nanowires 50 and 100 nm in diameter inside AAO matrix is established to be $1.4 \cdot 10^{10}$ and $9 \cdot 10^{8}$ cm^{-2} respectively. Contact problem of nanowire / electrode is investigated and contact optimization procedure is found. Electro conductivity of individual germanium nanowires within AAO is studied and compared with averaged conductivity over large amount of nanowires in array. Nearly all nanowires inside membrane are found to be electroconductive and exhibit intrinsic conductivity. Photoconductivity and photodynamics of Ge nanowire arrays inside AAO are investigated. Photoconductive properties are analyzed and ultra high resolution photosensitive matrix based on nanowire array inside AAO is proposed.

Electroconductivity of nanoparticle (Au) catalyst synthesized free Si and Ge nanowires is studied and nanowire / electrode contact area is simultaneously visualized. Electroconductivity of free nanowires is compared with electroconductivity of AAO template synthesized nanowires and it is found that in the first case it is much higher (10^{3}-10^{4} times) due to doping with Au atoms of catalyst nanoparticles. Nanoelectromechanical interactions of single semiconducting nanowires with metal electrodes are investigated. High elasticity (higher than elasticity of bulk material) of single nanowires is also demonstrated. Information on mechanical properties and acting forces was collected and used to propose and demonstrate some principles of nanoelectromechanical device (NEPROM memory element) based on single semiconducting nanowire.

Novel 3D DNA architecture of spatially distributed oligomer array on Au (111) surface is researched. DNA oligomer surface density can be varied in range 10^{10}-10^{11} cm^{-2} by changing the DNA concentration in coating solution. Structure of oligomer array is studied and vertical orientation of DNA molecules is proved. Viscoelastic behavior of DNA oligomers attached to solid surface is demonstrated. Electroconductivity of individual DNA oligomers was probed directly by conductive AFM tip and DNA oligomers found to be poor current conductors.

At the end of this work the properties of investigated materials are summarized and a possibility to combine DNA molecules and semiconducting nanowires into functional devices is discussed.

LIST OF PUBLICATIONS INCLUDED INTO THE THESIS

Paper I. B.Polyakov, B.Daly, J.Prikulis, V.Lisauskas, B.Vengalis, M.Morris, J.Holmes, D.Erts. High Density Arrays of Germanium Nanowire Photoresistors. *Advanced Materials* (in press).

Paper II. D.Erts, B.Polyakov, B.Daly, M.Morris, S.Ellingboe, J.Boland, J.Holmes. High Density Germanium Nanowire Assemblies: Contact Challenges and Electrical Characterization. *Journal of Physical Chemistry B*, *110*, 820-826, 2006.

Paper III. K.Ziegler, B.Polyakov, J.Kulkarni, T.Crowley, K.Ryan, M.Morris, D. Erts and J.Holmes. Conductive films of ordered nanowire arrays. *Journal of Material Chemistry*, 14, 4, 585 - 589, 2004.

Paper IV. K.Ziegler, D.Lyons, J.Holmes, D.Erts, B.Polyakov, H.Olin, K.Svensson, E.Olsson. Bistable nanoelectromechanical devices. *Applied Physics Letters*, 84, 20, 3957-4121, 2004. (Also selected for publication in *Virtual Journal of Nanoscale Science & Technology*, 9, 19, 2004)

Paper V. D.Erts, B.Polyakov, E.Saks, H.Olin, K.Ziegler, J.D.Holmes. Semiconducting nanowires: properties and architectures. *Solid State Phenomena*, 99-100, 109-116, 2004.

Paper VI. D.Erts, B.Polyakov, A.Lõhmus, R.Lõhmus, H.Olin, M.A.Morris, J.D.Holmes. Metallic and semiconducting nanowires studied by TEM-SPM. *Physics of Low-Dimensional Structures*, 3/4, 65-74, 2003.

Paper VII. B.Polyakov, D.Erts, U.Malinovskis, I.Muiznieks, E.Tuite. SPM studies of DNA architectures on Au(111) and mica surfaces. *Physics of Low-Dimensional Structures*, 3/4, 269-277, 2003.

Paper VIII. D.Erts, B.Polyakov, H.Olin, and E.Tuite. Spatial and mechanical properties of dilute DNA monolayers on gold imaged by AFM. *Journal of Physical Chemistry B*, 107, 3591-3597, 2003.

LIST OF RELATED PAPERS NOT INCLUDED INTO THE THESIS

N1. B.Polyakov, B.Daly, J. Xu, J.Holmes, D.Erts. Investigation of Semiconducting Nanowire Arrays inside AAO Solid Matrix using Atomic Force Microscopy and Scanning Electron Microscopy. *Manuscript*.

N2. B.Polyakov, J.Prikulis, L.Grigorjeva, D.Millers, V.Zauls, J.Holmes, D.Erts. Photoconductivity in Germanium Nanowire Arrays Incorporated in Anodic Aluminum Oxide. *Manuscript*.

N3. D.Erts, B.Polyakov, B.Redkins, J.Holmes. Force interactions and conductivity of Ge nanowire arrays encapsulated within oxidized alumina. *Proceedings of the 1st Latvian Conference on Nanotechnology*, Riga, Latvia, 83-86, March 30-31, 2005.

N4. D.Erts, B.Polyakov, H.Olin, E.Tuite. Spatially Distributed 2-Dimensional DNA Arrays on Au (111): AFM Characterisation. *Latvian Journal of Physics and Technical Sciences,* 4, 63-72, 2001.

N5. M.Knite, V.Teteris, B.Polyakov, D. Erts. Electric and elastic properties of conductive polymeric nanocomposites on macro- and nanoscales. *Materials Science and Engineering C*, 19, 1-2, 15-19, 2002.

N6. M.Knite, V.Teteris, I.Klemenoks, B.Polyakov and D.Erts. Nanostructure carbon black - polyisoprene composites as prospective strain sensor materials: macro- and nanoscale studies. *Fifth International Workshop on Nondestructive Testing and Computer Simulations in Science and Engineering, SPIE* vol. 4627, 113-117, 2002.

N7. M.Knite, V.Teteris, B.Polyakov, D.Erts. Exstraconductive carbon black – superelastc polymer composite as prospective deformation sensormaterial: investigations in macro- and nanoscales. *Scientific Proceedings of RTU "Material Science and Applied Chemistry"*, 1: (2) 39-47, 2001.

N8. R.Dobulans, D.Cepite, E.Fonavs, I.Muzikante, A.Tokmakov, D.Erts, B.Polakov. Studies of host-guest thin films of corona poled betaine type polar molecules by Kelvin probe technique and atomic force microscopy, *Macromolecular Symposia*, 212, 1, pp. 421-426, 2004.

N9. I.Muzikante, D.Cepite, E.Fonavs, A.Tokmakov, D.Erts, B.Polakov. Oriented polar molecules incorporated in PMMA polymeric films: Kelvin probe and atomic force microscopy characterization, *Latvian Journal of Physics and Technical Sciences*, 3, 49-55, 2003.

N10. I.Muzikante, D.Cepite, E.Fonavs, A.Tokmakov, D.Erts, B.Polakov. Incorporated Oriented polar molecules in PMMA polymeric films: characterization by Kelvin probe technique and atomic force microscopy. *IEEE Transactions on Elektrets, Proceedings of 11th International Symposium on Electrets ISE-11*, 383-385, 2002.

The results of this work were reported at 20 International conferences (22 reports) and 6 local conferences (15 reports), and published in proceedings and abstract books:

1. International Conference TNT-2005 (Trends in Nanotechnology), Oviedo, Spain, 29 August – 2 September, 2005.
B.Polyakov, B.Daly, J.Prikulis, B.Vengalis, J.Holmes, D.Erts. Photoconductive Properties of Germanium Nanowires Incorporated in Anodic Aluminium Oxide Membranes.

2. 10th INTEL Academic Forum, May 18-20, Gdansk, Poland, 2005.
D.Erts, B.Polyakov, B.Daly, J.Holmes. Conductive and Photoconductive Properties of Ge Nanowire array in AAO.

3. NSTI Nanotechnology Conference & Trade Show, Anaheim, CA, USA, May, 2005.
B.Daly, J.Kulkarni, K.Ziegler, T.Crowley, D.Erts, B.Polyakov, M.Morris, J.Holmes. Conductive Films of Ordered Nanowire Arrays.

4. 4th ESF Nanotribo workshop, June 19-22 Porquerolles, France, 2005.
D. Erts, B. Polyakov, B. Redkins, J.D. Holmes. Electrostatic, friction forces and conductivity of Ge nanowire arrays encapsulated within oxidized alumina.

5. 21st Scientific conference of University of Latvia, Riga, 7-9 February, 2005.
- B.Polyakov, B.Daly, Y.Prikulis, L.Grigorjeva, D.Millers, J.Holmes, D.Erts. Electroconductive and photoelectroconductive properties of Ge nanowires inside AAO membranes.
- B.Redkin, B.Polyakov, J.Holmes, D.Erts. Nanotribology on Ge nanowire architectures.
- U.Malinovskis, A.Pastare, B.Polyakov, I.Muižnieks, D.Erts. Controlled selfassembling of DNA networks on mica surface.
- D.Erts, J.Prikulis, B.Polyakov. New ES structural funds and home-made instruments in the Institute of Chemical Physics.

6. 1st Latvian Conference on Nanomaterials and Nanotechnologies, Riga, Latvia, March 30-31, 2005.
- B.Polyakov, B.Daly, Y.Prikulis, L.Grigorjeva, D.Miller, J.H.Holmes, D.Erts. Conductive and photoconductive properties of Ge nanowires in anodic aluminium oxide membranes.
- B.Redkins, B.Polyakov, J.H.Holmes, D.Erts. Local electrostatic, friction forces and conductivity of Ge nanowire arrays encapsulated within oxidized aluminium.
- D.Erts, B.Polyakov, J.H.Holmes. Nanoelectromechanical devices.
- R.Udris, L.Lauks, J.H.Holmes, B.Polyakov, D.Erts. Light and radiation detection by germanium nanowire arrays.

7. Int. Conference TNT-2004, (Trends in Nanotechnology), Segovia, Spain, September 13-17, 2004.
B.Polyakov, D.Erts, J.Holmes. Complex studies of Ge nanowire arrays in oxidized alumina membranes.

8. Nordic-Baltic SPM workshop, Trondheim, Norway, June 15-17, 2004.
- B.Polyakov, D.Erts, J.Holmes. AFM studies of conductive Ge nanowire arrays in oxidized alumina membranes.
- D.Erts, H.Olin, J.Holmes, B.Polyakov, A.Lohmus. Electrical and mechanical properties of nanowires studied by SPM.

9. SPM - 2004 International Workshop, Nizhny Novgorod, Russia, May 2-6, 2004.
U.Malinovskis, A.Pastare, B.Polyakov, I.Muiznieks, D.Erts. AFM studies of DNA networks on mica surface.

10. 20th Scientific conference of University of Latvia, Riga, February 16-18, 2004.

- B.Poļyakov, L.Lauks, R.Udris, J.Holmes, D.Erts. Thin films of conductive ordered Ge nanowire arrays.
- D.Erts, B.Polyakov, E.Saks, A.Patmalnieks, H.Olin, J.Holmes. Metal and semiconducting nanowires and architectures.

11. 8th Conference of Latvian Physical Society, Jelgava, Latvia, July 1, 2003.
D.Erts, B.Poļakovs, E.Saks, U.Maļinoskis. Nanocomponents: properties, architectures, devices.

12. Scanning Probe Microscopy – 2003 International workshop, Nizhny Novgorod, Russia, March 2-5, 2003.
- B.Polyakov, D.Erts, U.Malinovskis, I.Muiznieks, E.Tuite., SPM studies of DNA architectures on Au(111) and mica surfaces.
- D.Erts, B.Polyakov, A.Lõhmus, R.Lõhmus, H.Olin, J.D.Holmes. Properties of metallic and semiconducting nanowires studied by TEM-SPM.

13. E-MRS 2003 Fall Meeting, Warsaw, Poland, September 15-19, 2003.
D.Erts, B.Polyakov, E.Saks, H.Olin, J.D.Holmes. Semiconducting nanowires: properties and architectures.

14. II ESF-Nanotribology Workshop, Antalya, Turkey, October, 2003.
D.Erts, B.Polyakov, E.Tuite. Force interactions between AFM tip and individual DNA oligomers.

15. 19th Scientific conference of University of Latvia, Riga, February 10-12, 2003.
- B.Polyakov, D.Erts, U.Malinovskis, I.Muiznieks, E.Tuite. DNA macromolecular architectures: creation and properties investigation.
- D.Erts, B.Polyakov, A.Truhins, L.Skuja, A.Patmalnieks, K.M.Ryan, J.D.Holmes. Investigation of 3D semiconducting nanowire architectures using TEM, AFM and optical methods.
- U.Maļinovskis, I.Muižnieks, B.Polyakov, D.Erts. DNA macromolecular architectures on solid surfaces.

16. Nordic-Baltic SPM workshop, Tartu, Estonia, May 29-31, 2002.
- D.Erts, J.D.Holmes, D.Lyons, M.A.Morris, H.Olins, E.Olsson, B.Polyakov, L.Ryen, K.Svensson. Properties of silicon nanowires studied by TEM-STM.
- B.Polyakov, D.Erts, E.Tuite, H.Olin, M.Knite. Conductive and mechanical properties of 2-dimensional DNA-arrays and electroconductive polymer composites.

17. 15th Inter. Congr. on Electron Microscopy. Durban, South Africa, 1-6 september, 2002.
D.Erts, H.Olin, B.Polyakov, L.Ryen, E.Olsson, J.Holmes. Conductive and mechanical properties of silicon nanowires investigated in situ by TEM-SPM.

18. International conference on nanometer scale science and Technology, 21st European conf. On Surface Science, Malmö, Sweden, June 24-28, 2002.
D.Erts, J.D.Holmes, D.Lyons, A.A.Morris, H.Olin, E.Olsson, B.Polyakov, L.Ryen, and K.Svensson. Solution-Grown Silicon Nanowire Studied By TEM-STM.

19. International Sc. Conf. on Biomedical Engineering and Microtechnologies, RTU, Riga, Latvia, October 10 - 14, 2002.
D.Erts, B.Polyakov, E.Tuite. Conductive and mechanical properties of DNA arrays.

20. 18th Sc. Conf . of ISSP University of Latvia, February 2002.
D.Erts, B.Polyakov, H.Olin. Mechanical properties and conductivity of single silicon nanowires measured by scanning tunneling microscope compatible with transmission electron microscope.

21. International Sc. Conf. on Biomedical Engineering and Microtechnologies, RTU, Riga, Latvia, October 10 - 14, 2002.
D.Erts, B.Polyakov J.D.Holmes, H.Olin. Properties of silicon nanowires.

22. Adriatico Research Conference on Interaction and Assembly of Biomolecules, Trieste, Italy, 27-31 August, 2001.
B.Polyakov, D.Erts, E.Tuite, H.Olin. Force and conductivity measurements on DNA-arrays and MCH monolayers on Au(111) surface with cAFM.

23. Second International Conference on Scanning Probe Spectroscopy, Hamburg, Germany, July 19 -22, 2000.
D.Erts, B.Polakov, H.Olin, T.Vajakas, E.Tuite. Tunneling and force spectroscopy of self assembled DNA monolayers on Au(111) abstract,

24. Eleventh International Conference on Mechanics of Composite Materials, Riga, Latvia, June 11 -15, 2000.
D.Erts, B.Polakov, and E.Tuite. Spatial, Mechanical, Conductivity Characterization of Self-Assembled DNA Arrays on Au(111) by Atomic Force Microscopy.

25. Nordic-Baltic SPM workshop, Goteborg, Sweden, June 5-7, 2000.
B.Polakov, D.Erts, H.Olin, T.Vajakas, E.Tuite. Conductive and Nanomechanical SPM Characterization of Self Assembled DNA Arrays on Au(111).

26. Int. seminar "Medical Engineering and Physics: Science, Practice, Busyness", Riga, 6-9 October, 1999.
D.Erts, E.Tuite, B.Polyakov. Structure and conductive properties of self assembled DNA by scanning probe microscopy.

Contents

1. Introduction

2. SPM principles

3. Ge nanowire arrays inside AAO

4. Nanoparticle catalyst synthesized free Ge and Si nanowires

5. 3D DNA arrays on Au(111)

6. Possible applications

Appended papers

LIST OF ABBREVIATIONS

1D	One Dimensional
2D	Two Dimensional
3D	Tree Dimensional
AAO	Anodized Alumina Oxide
AFM	Atomic Force Microscope
C-AFM	Conductive probe Atomic Force Microscope
CMOS	Complementary Metal Oxide Semiconductor
CVD	Chemical Vapor Deposition
DNA	Deoxyribonucleic Acid
EDX	Energy Dispersive X-ray analysis
FET	Field Effect Transistor
ITO	Indium Tin Oxide
LED	Light Emitting Diode
MCH	Mercaptohexanol
NEMS	Nano Electro Mechanical Systems
NEPROM	Non Erasable Programmable Read Only Memory
NW	Nanowire
SCF	Supercritical Fluid
SPM	Scanning Probe Microscopy
STM	Scanning Tunneling Microscope
TEM-STM	Transmission Electron Microscope combined with Scanning Tunneling Microscope
VLS	Vapor Liquid Solid

CHAPTER 1

INTRODUCTION

1.1. Main problems to solve

Technical progress evolves parallel to the invention of new materials and novel technologies. In past few decades silicon technologies provided a great advance of microelectronics resulting in birth of super fast computers and super small microprocessors. Nevertheless, in near future, both physical and economic constraints are expected to limit the continued miniaturization of CMOS (Complementary Metal Oxide Semiconductor) microelectronic devices based on current top-down photo lithography techniques [1]. That is why new methods and concepts for creation of integrated circuits will be required. Solution search is running on different levels and in numerous directions. There is a great need in creation of new nanomaterials and tailoring their characteristics for specific applications. Researchers are developing alternative microelectronic devices based on completely new materials and non-lithographic fabrication methods, novel device architectures and principles of its work [2, 3, 4].

In recent time nanoscale materials such as carbon nanotubes, metal and semiconducting nanowires, nanoparticles, fullerenes, nanodots were studied in many aspects of their properties. However, the technology of integration of many individual *nanoobjects* (0D or 1D nanostructures) into functional devices has not yet been sufficiently developed. This problem consists of two parts. First one is the precise positioning of nanoobjects. A very promising approach of solving this problem is application of self-assembling principles when nanoobjects spontaneously assemble into ordered 2D or 3D architectures. The second challenge arises if one would integrate nanoobjects into an electrical circuit. At this moment the only available technology for the permanent contacting is the electron beam lithography, which is expensive, complicated and underproductive. Nanotechnology proposes utilization of nanowires for electrical addressing of individual nanoobjects. *Nanowires* (NW) are defined here as elongated structures of high aspect ratio with a diameter of nanometer size (1D nanostructures). Both organic and inorganic nanowires are believed to be components of future nanodevices [5, 6].

In this PhD work two types of nanowire materials are studied: semiconducting nanowires (Si, Ge) and DNA molecules. Structure, electroconductive and mechanical properties of these materials are investigated. The work is focused on three dimensional self-assembled nanowire architectures. Ordered germanium nanowire arrays synthesized inside porous AAO and 3D self-assembled architectures of DNA molecules and their application possibilities are investigated in this work.

1.2. Semiconducting Nanowires

Utilization of inorganic materials will most likely continue to dominate the electronic industry in the nearest future. In particular, Si and Ge semiconducting nanowires are well compatible with conventional integrated circuit technology [7, 8]. Application of nanowires has a great advantage as inexpensive and nonlithographic technology for creation of nanometer size structures. A single semiconducting nanowire can work as an entire device as already has been demonstrated by some researchers [9, 10, 11].

Semiconducting nanowires usually have crystalline structure, with diameter from a few nanometers to hundreds of nanometers and length up to hundreds of micrometers. Atoms in these crystals are covalently bonded, and thus their form highly rigid and robust nanoobjects. Most popular method of nanowire synthesis is so called VLS (vapor-liquid-solid) approach in combination with CVD (chemical vapor deposition) or laser ablation [12]. The essence of the VLS method is for producing nanowires is the nucleation and growth of the nanowires from metal catalyst nanoparticles. An alternative approach is template assisted nanowire synthesis. Porous templates can be filled using nanowire precursor material either by thermal decomposition of precursor, which is fed in gaseous or liquid phase, or electrochemically deposited [13].

Hiruma et al. working at Hitachi pioneered in nanowire research and application during the early to mid 1990s [14]. He demonstrated application potential of III-V group semiconductor nanowires, their good optical properties; possibility to create pn-junctions inside nanowires, which can be utilized to produce light-emitting diodes [15]. Various fascinating works have been performed by Lieber et al., who proposed and demonstrated the applicability of n- and p-doped Si nanowires for assembly of logic circuits. Lieber has also suggested and demonstrated light emitting transistor based on p-Si / GaN, CdS, CdSe nanowire-nanowire contacts [16].

It should be noted that most of the previously demonstrated nanowire (and nanotube) based devices have two dimensional (2D) design. For example figure 1.2.1(a) shows nanotube based nanorelay similar to one as reported in [17]. It means, that in spite of ultra small diameter of nanowires (down to few nanometers), the real device dimensions are measured in micrometers and cannot help in electronic chip miniaturization. Multilayer planar NW-based device architecture, which extends in the third dimension, may thus enhance the device complexity. Unfortunately this requires complicated and expensive technology. Most attractive solution is engineering of three dimensional (3D) NW-based devices. This way a high packing density of nanodevices can be achieved (figure 1.2.1(b)). Therefore investigation of 3D nanowire array materials is important for development of novel nanoelectronic and nanoelectromechanical devices [1].

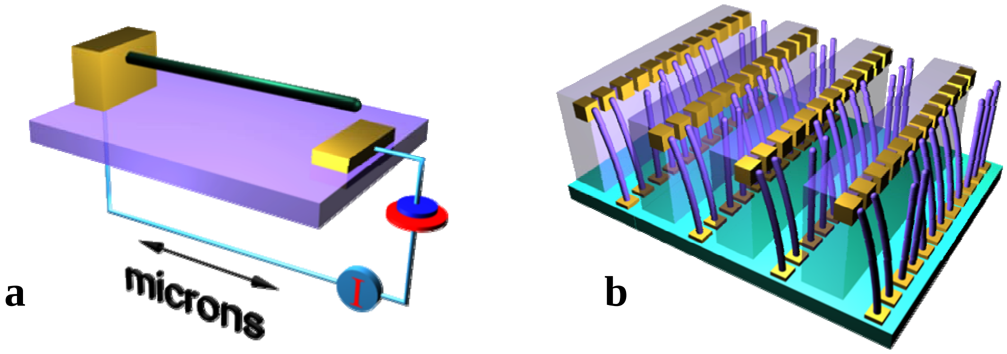

Figure 1.2.1. (a) - schematics of 2D design of a nanorelay; (b) - hypothetical 3D assembly of nanorelay array.

1.2.1. 3D nanowire arrays. Assembly of nanoobjects in real devices where billions of nanocomponents are required is one of the most challenging problems in nanotechnology. Nanoscale arrays of semiconducting nanowires in porous materials have been widely studied as a partial solution to this problem. The ability to pack high densities of homogeneous or complex nanowires into 3D nanowire arrays, and control their transport properties is expected to produce a new generation of electronic circuits and array-based nanodevices. Nanometer pores and channels in mesoporous solids [18], polycarbonate track membranes [19] and nanochannel array glasses [20] have been recently used as templates for nanowire formation.

Recently AAO has been in the focus of intense research as a template for nanowire encapsulation. Porous alumina is a unique material in a number of aspects. It is possible to prepare AAO of any size and shape by anodic oxidation of aluminium surfaces in polyprotic aqueous media. AAO have an ordered array of hexagonal cells with pore diameters ranging between 10 and 200 nm in diameter. Pore densities as high as 10^8 to 10^{11} cm^{-2} have been reported with film thickness varying from 0.1 to 250 μm [21, 22]. AAO is optically transparent and thermodynamically stable up to 1000 ^{o}C. The well-ordered pores in AAO offer tremendous potential as hosts for various materials and have been attracting considerable interest as templates for creation of nanowires [23, 24].

Most measurements on nanowire electrical properties reported in the literature were performed on free nanowires. In particular, transport properties and contact problems of individual Si nanowires were studied in [25, 26]. Dai et al. has investigated the effects of surface states in operation of Ge nanowire-based FETs [27]. Korgel et al. has been working on synthesis and electrical contacts of Ge nanowires grown using a supercritical fluid-liquid-solid mechanism [28]. However, there is little data on electrical characterization of semiconducting nanowire arrays inside AAO [29] and to our knowledge no data on germanium nanowire arrays. Elaboration of methods to contact semiconductor nanowires and contact optimization are essential for most nanoelectronic devices.

A perspective field of semiconducting nanowires and nanodots application is development of novel equipment for optoelectronics and telecommunication [30]. Investigation of photoconductivity processes in such structures provides information necessary for creation of new devices for optical-to-electronic signal conversion. Most photoconductivity measurements have been performed on direct gap materials such as InP [31], ZnO [32], SnO_2 [33], CdSe [34] and GaN [35] nanowires. Although these materials offer superior photoconductivity properties in comparison to elemental semiconductors (Si and Ge), their integration into functional devices is predicted well into the future [1]. Optical studies on elemental semiconducting nanowires have focused primarily on the confinement effects using photoluminescence measurements [36, 37]. Recently however, Park et al. initiated photoconductivity measurements on indirect gap semiconducting nanowire systems by performing optical scanning measurements on photocurrent in individual Si nanowire FETs [38]. There have been no studies on photoconductivity of elemental nanowire arrays until now.

In first part of this work (chapter 3) Ge nanowire arrays inside AAO were studied. Primary task was to prove that nanowires are electroconductive and possess semiconducting properties. Second task was to investigate the photoconductive properties of nanowire arrays.

1.2.2. Individual nanowires. Most of the earlier performed electrical characterization studies were done on free nanowires created by VLS synthesis method. The second part of this work (chapter 4) concentrates mainly on investigation of electroconductive properties of Ge and Si nanowires grown on metal catalyst nanoparticles by VLS method. Properties of these Ge nanowires are compared to AAO template synthesized Ge nanowires.

Additional aim in this study was research of nanowire force interactions with metal electrodes. Traditionally, mechanical devices are considered to be slow. However, utilizing nanoscale structures for mechanical devices could achieve GHz or

THz resonance frequencies making NEMS faster than current electronic devices [39]. There were few studies before on the force interactions of nanotubes [40] and no studies on the force interactions of nanowires with electrical contacts. Such studies provide important parameters for development of nanoelectromechanical systems (NEMS). To date, researchers have focused on use of carbon nanotubes as building blocks for the construction of NEMS due to their mechanical strength [17, 41]. Semiconductor nanowires, such as Si or Ge, however, offer the distinct advantage over carbon nanotubes in that their sizes and electronic properties can be controlled in a predictable manner during their synthesis.

It was also shown in this work how the semiconductor nanowire can be utilized in the construction of a nanoelectromechanical programmable read-only memory (NEMPROM) device. Detailed information about both electroconductivity and mechanical properties of nanowires is important for the development of 3D integrated NEMS, which can be utilized for high density memory engineering.

1.3. DNA arrays

DNA or deoxyribonucleic acid is a famous molecule of Life. In nature it is used to encode genetic information. DNA consists of two chains of chemical units called nucleotides. A nucleotide consists of a base, either a purine or pyrimidine, to which sugar phosphate group attached. The bases in DNA are of four different types: adenine and guanine (purines) and thymine and cytosine (pyrimidines). The two nucleotide chains are attached to each other by hydrogen bonding between specific purine base on one strand and a specific pyrimidine base on the other strand. In DNA, adenine binds to thymine and guanine to cytosine. This is called a base pair arrangement. Thus adenine on one strand is *complementary* to thymine on the other strand and guanine on one strand is *complementary* to cytosine on the other strand. Double stranded DNA exists in cell in the form of a helix. DNA diameter is about 2 nm and 10 nucleotides have length 3.4 nm. As a polymer DNA molecule may have infinite length [42].

In nature, self-assembly processes are one of the main driving forces for the bottom-up creation of complex biological structures. Self-assembly is one of the basic concepts of nanotechnology and many mechanisms are borrowed from Nature. In particular, the self-organization of nanometer-scale building blocks by biomolecular recognition provides universal approach to the synthesis of structured architectures on multiple length scales [43, 44]. Spontaneous assembly and selective encoding of such nanostructured components has been achieved with streptavidin/biotin binding [45] and antibody/antigen matching [46]. However, to date, oligonucleotide base pairing is the most thoroughly studied encoding system [47] and DNA is proposed as an important tool for nanomaterials engineering [48]. Most studies have used DNA duplex formation via complementary recognition to assemble networks of spherical nanoparticles with identical physical properties (metallic, magnetic, semiconducting) or alternatively to anchor these nanoparticles to macroscopic substrates.

DNA molecules are much more flexible in comparison with semiconducting nanowires, they may be easily bended and used as wires for connection of semiconducting nanowires (or other nanocomponents) into nanodevices. Hypothetic schemes of nanocomponents assembling and connection using 3D DNA architectures are shown at figure 1.3.1.

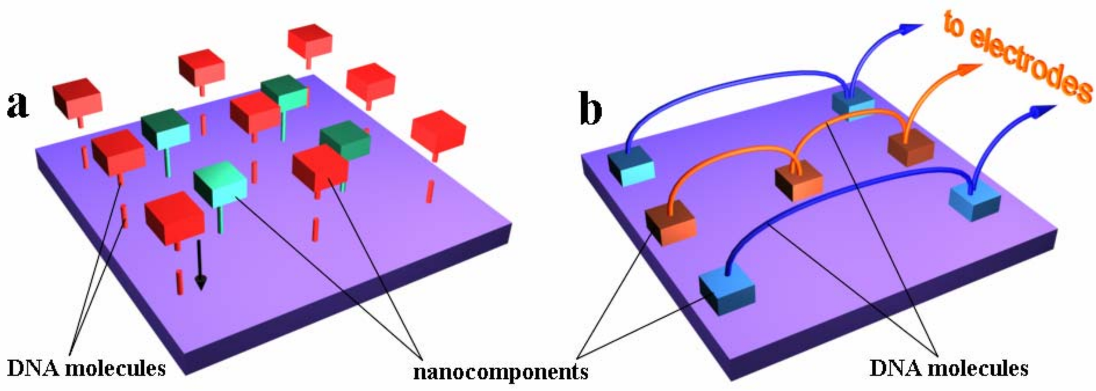

Figure 1.3.1. Hypothetic application of DNA molecules for programmable assembling of nanocomponents on solid surface (a); for electrical connection of nanocomponents into electrical circuits (b).

Self-assembled monolayers of DNA with controlled spatial distribution on surfaces may have many applications. Arrays of DNA at surfaces are most familiar as tools for functional genomics in the form of DNA chips. Another potential application is use of DNA arrays as foundation templates for the construction of nanostructured materials *via* programmed self-assembly, where variable spatial distribution is absolutely critical to obtain desirable allocation of nanoobjects. Learning how to control the formation of 2D and 3D assemblies, i.e. combining molecular scale building blocks into well-defined meso- and macroscopic structures, is the essence of nanotechnology and materials chemistry.

Third part of this study (chapter 5) was performed on spatially distributed 3D DNA oligomer arrays attached to gold surface. First aim of this topic was to investigate structure of created DNA architecture and distribution of individual molecules. Second aim was to probe electroconductivity of DNA oligomers and test the hypothesis of DNA molecule metallic conductivity. In recent literature [49, 50] there has been considerable debate regarding whether DNA behave as a "molecular wire" and mediate vectorial transfer and/or transport of electrons via a π-stack of the basepairs or not. A number of conflicting studies on direct conductivity measurements have been reported, as well as variety of theoretical models. It should be noted, that densely coated DNA monolayers on the surface have been described, for example in [51]. The spatially distributed DNA arrays are specially designed for conductive probe AFM measurements, then the AFM tip statistically contacts only single DNA molecule.

1.4. Layout

The promotion work is prefaced with the abstract, list of publications and conferences, where the main results were presented. The work is organized into the following chapters:

- Chapter 1, "Introduction", where the short historical review is given and the importance of chosen theme is argued;
- Chapter 2, "SPM principles", introduces some basic information about used instruments;
- Chapter 3,"Ge nanowire arrays inside AAO" presents the first part of my study, where electroconductive and photoconductive properties of template synthesized nanowires are described;
- Chapter 4, "Nanoparticle catalyst synthesized free Ge and Si nanowires", presents the second part, where electroconductive and mechanical properties of nanoparticle catalyst synthesized free nanowires are revealed;
- Chapter 5, "3D DNA arrays on Au(111)", is the third part of the study, where structure of this DNA architecture is described and electroconductivity of DNA oligomers probed;
- Chapter 6, "Possible applications", where utilization of Ge nanowires and DNA molecules discussed;
- Chapter 7, "Conclusions and Thesis", summarizes the work;
- Chapter 8, "References", where bibliography is given.

Work is appended with copies of the included papers. The promotion work contains 62 pages, 54 figures, 4 tables and 89 references.

CHAPTER 2

SPM PRINCIPLES

SPM is a common name for a family of related techniques, such as STM (Scanning Tunneling Microscope), AFM (Atomic Force Microscope or Scanning Force Microscope), SNOM (Scanning Near field Optical Microscope), TEM-STM (STM combined with Transmission Electron Microscope) and others.

2.1. STM principles

STM principle is illustrated by figure 2.1.1. STM probe is a sharp metal tip. STM sample should be electrically conductive also. Voltage is applied between sample and tip. Current is an operating signal in STM. It grows exponentially with decreasing tip-sample distance. The tunneling current starts to flow when the tip is approached to the surface at distance of several angstroms. Feedback system is keeping the current and tip-sample distance constant. When tip starts to scan the surface, it follows the surface topography. Any topographical feature on the surface causes the change of the tunneling current. The feedback system tries to readjust the tip position to keep tunneling current constant. System sends compensative voltage to Z-electrode of piezoscanner (read more about piezoscanner in 2.4.2 section) to recover the nominal tip-sample separation. At proper feedback parameters tip never touches the sample surface. Piezoscanner deformation is proportional to applied voltage. At each point of scanning area in X,Y plane the voltage to Z piezo electrode is recorded and thus 3D surface topology can be reconstructed. This description corresponds to constant current regime.

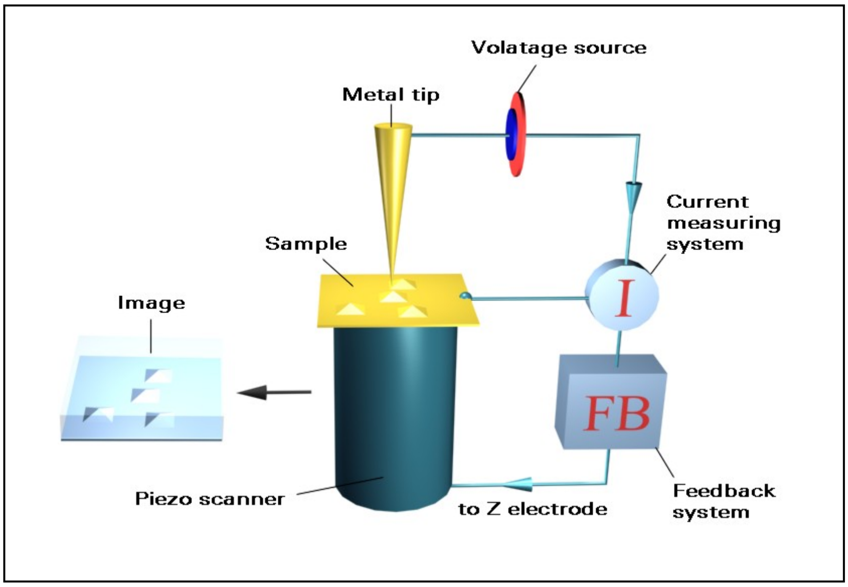

Figure 2.1.1. STM principles.

Extremely high resolution of STM technique is possible due to exponential tunneling current dependence on the electrode separation distance. Tunneling current changes by an order of magnitude changing distance by 1 Å. The following formula can help to understand physical interpretation of STM images [52]:

$$I \propto U \cdot n_t(E_F) \cdot n_s(E_F, r_0) \cdot \exp(2\kappa R), \qquad 2.1.1$$

where U – voltage bias, E_F is the Fermi energy; the decay rate equal to $\kappa=(2m\phi)/h$ and ϕ is the effective local potential barrier height, m – electron mass, h – Plank constant; R is the effective tip radius, and r_0 is the center of the curvature of the tip (see figure 2.1.2); $n_t(E_F)$ is the density of states at the Fermi level for the tip; $n_s(E_F, r_0)$ is the surface local density of states at the Fermi level E_F evaluated at the center of the curvature r_0 of the tip. Thus the STM images obtained at low bias in the constant current mode therefore represent contour maps of constant surface LDOS at E_F evaluated at the center of curvature of the tip.

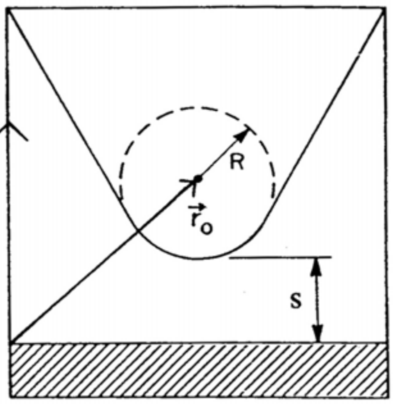

Figure 2.1.2. Schematic picture of tunneling geometry [52].

The electron wave function decay exponentially in the z direction normal to the surface towards the vacuum region, thus [52]:

$$n_s(E_F, r_0) \propto \exp[-2\kappa(s+R)], \qquad 2.1.2$$

where s is the distance between the sample surface and the end of the tip. Therefore, the tunneling current is exponentially dependent on the distance between tip and sample $I \sim \exp(-\kappa s)$, as it was already mentioned above.

2.2. AFM principles

AFM is based on force interaction between a tip and a sample. It is known that repulsive atomic force dominates at small distances and attractive force at large distances. AFM can be operated in repulsive, attractive, and in mixed regimes. Corresponding modes are called the contact mode, the non-contact mode and the taping mode.

Figure 2.2.1 demonstrates AFM work principle. Probe is a microscopic cantilever with a sharp tip at its end. Laser beam falls onto the end of cantilever and reflects to two- or four segment photodetector. When the tip touches the sample surface, cantilever bends and reflected laser beam displaces. The laser displacement is registered by photodetector and is used as operating signal. Feedback system keeps cantilever bending constant (bending is linearly proportional to applied force). Scanning procedures are similar as in STM. This setup corresponds to contact mode regime. In tapping and non-contact modes the cantilever is oscillating with kHz frequency. The cantilever oscillation amplitude decreases at increasing tip-sample interaction and used as a operating signal.

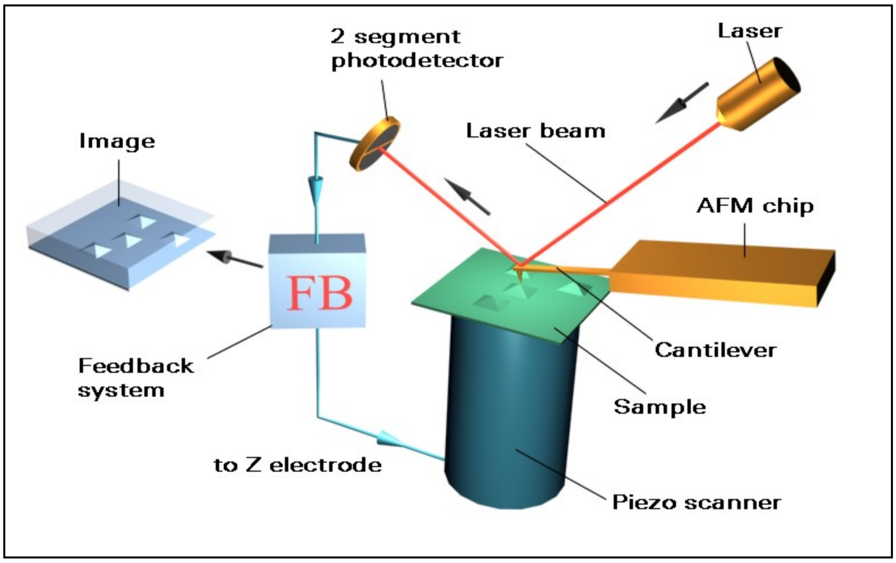

Figure 2.2.1. AFM principles.

AFM is more universal than STM. AFM does not need electroconductive sample. It works as good on metal surfaces as on insulating one. However we can use conductive tips in AFM case, apply some voltage between sample and tip (as in STM case) and measure the passing current as an additional channel. This technique often is called C-AFM or conductive AFM. If we use four segment photodetector, then lateral or friction force can also be detected. Application example of simultaneous detection of topography, conductivity and friction force will be shown in next chapter.

Tip-sample interaction force consist of two components [52]. The first, denoted as F_{ion}, originates from the Coulomb repulsion between the ion cores, and the second, denoted as F_{el}, is due to the interaction of valence electrons with the ion cores (figure 2.2.2). At small tip-surface separations, the repulsive force F_{ion} is stronger and varies more rapidly with the position of the outermost tip atom than does F_{el}. Therefore, AFM operated in the repulsive contact mode is expected to be mainly sensitive to the repulsive Coulomb interaction between the ion cores of the tip and those of the sample surface. Thus, AFM image in contact regime represent direct probing the position of sample surface atoms ion cores. As the tip-surface separation is increased, F_{el} decays more slowly than F_{ion} and $F_{total}=F_{ion}+F_{el}$ changes its sign, leading to a net attractive force. In this (noncontact) regime, the AFM would mainly probe the total charge density distribution of the sample surface rather than ion-ion repulsion.

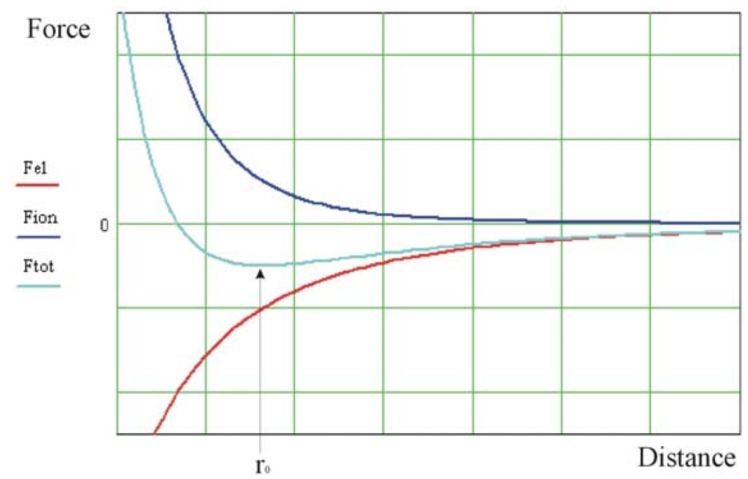

Figure 2.2.2. Graphic simulating F_{ion}, F_{el} and F_{total} dependence on distance between two atoms. Arrow indicates equilibrium position r_0 of atoms nucleus.

2.3. TEM-STM principles

TEM-STM is a combination of TEM microscope and STM designed as TEM holder. Piezoscanner of STM is used as nano manipulator in this system. Electron optics of TEM used for visualization of investigated object, which can be electrically characterised and simultaneously visualised. In case of semiconducting nanowire investigation, force interactions also can be studied. Semiconducting nanowire works as elastic AFM cantilever and its bending can be directly visualized by TEM.

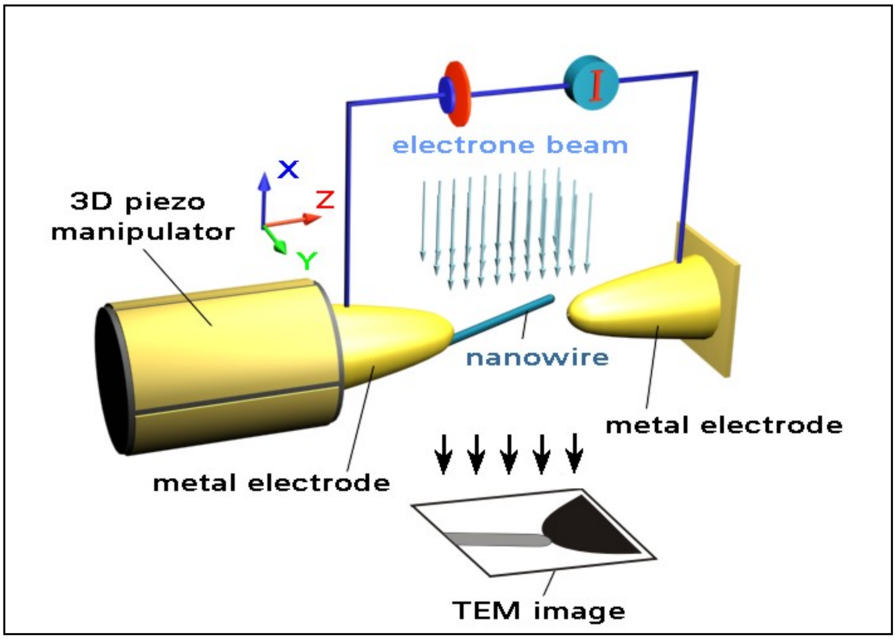

Figure 2.3.1. Principles of TEM-STM.

2.4. SPM design and instrumentation

Scanning Probe Microscope includes mechanical part, control electronics, computer and operating software. The mechanical part of SPM could be placed in vacuum chamber and criocooled to achieve atomic resolution. Ambient SPM usually are placed onto vibroisolating system.

2.4.1. Vibroisolating system

For atomic resolution mechanical vibrations level (in vertical direction) has to be less than 0.01 Å. Ordinary level of floor vibrations has amplitude about 0.1-1 μm. Consequently, it is necessary to build a vibrations isolating system, which is able to minimize vibrations level at least by six orders of magnitude. To minimize vibrations constructor should take into consideration the following recommendations. Microscope should be compact and rigid to have the resonance frequency as high as possible (typical ~kHz). The resonance frequency of vibroisolating system, on the contrary, should be as low as possible (~Hz). Microscope itself represents a high pass filter, while the vibroisolating system is a low pass filter. When microscope stands on damping platform, we have a mechanical system, which minimises vibrations of wide spectrum (figure 2.4.1.1). Many vibroisolating systems (pneumatic, superconductive, electromagnetic suspension and others) are available on the market.

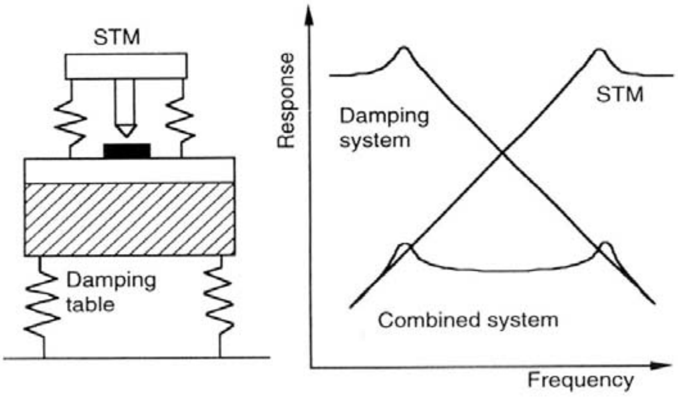

Figure 2.4.1.1. Simplified model of an STM and a vibration-damping table. Graphic shows the combined amplitude transfer function of the two providing a high attenuation of vibrations over the whole spectrum [53].

2.4.2. Mechanics

STM microscope design is quite simple. It consists of a probe, piezoscanner and coarse approach mechanism (manual approach screws and stepper motor). In

AFM case it is necessary to have a system for registration of cantilever bending (laser and detector).

Piezodrive (or piezoscanner) is used to move a sample respective to tip in X-Y plane (same with sample surface plane) and in Z-direction. Maximal movement of piezodrive in Z direction does not exceed few µm, that is why a coarse approach system is used to bring probe close to surface (in STM case distance between tip and sample is about 10 Å). Usually the coarse approach is realized by with electric stepper motor. Final fine approach is executed by piezodrive.

Popular piezoscanner is piezoceramics in the form of hollow cylinder (figure 3.4.2.1 a). This design is compact and has high oscillating eigenvalues. External surface of piezo ceramic cylinder is coated by four metal electrodes: +X, -X, +Y, -Y. Internal surface is coated by one electrode – Z. Figure 2.4.2.1 b-e demonstrates piezodrive deformations in X, Y direction according to the voltage applied to electrodes.

Deformations can be described by the following formulas [53]:

$$\Delta x = \Delta y = 2\sqrt{2} d_{31} V L^2 / \pi D h, \qquad 2.4.2.1$$

$$\Delta z = d_{31} V L / h, \qquad 2.4.2.2$$

where L is length of piezotube, h – thickness, D – diameter and V – applied voltage. d_{31} – is piezoelectric constant of material. In advanced systems movements of piezoscanner are controlled by external sensor. It eliminates most piezoceramics weaknesses resulting in uncertainty of tip position and image distortions.

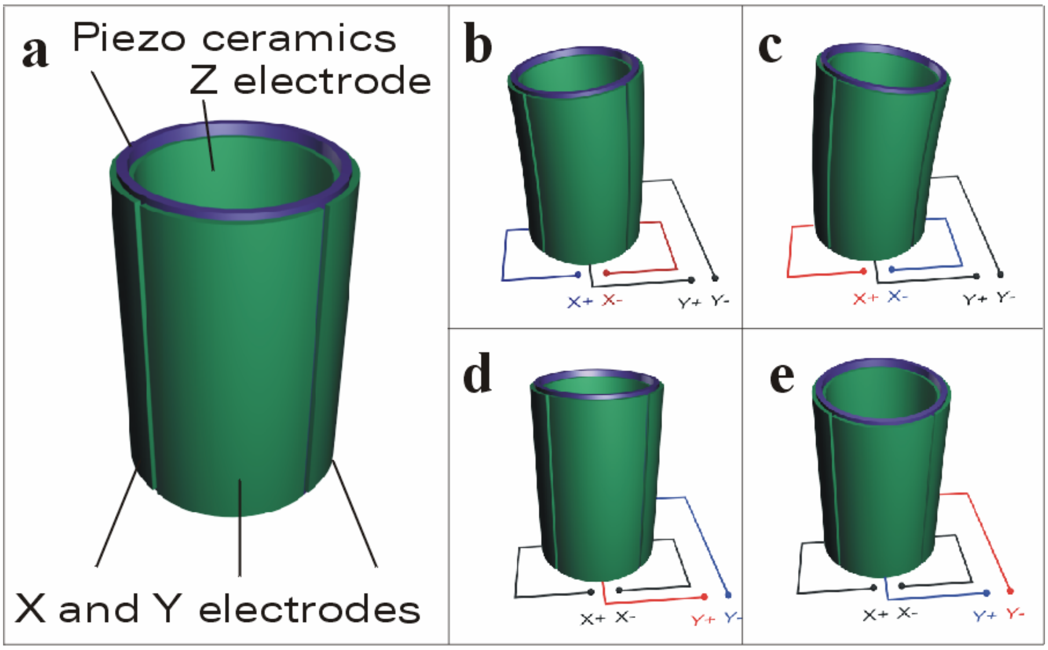

Figure 2.4.2.1. Piezoscanner (a) and its deformations depending on applied voltage (b-e).

2.4.3. Electronics

Electronic part of SPM should be designed as precise as mechanical part. The quality of signal processing by feedback has critical significance for proper work of microscope resulting in precise positioning of probe. Block diagram of SPM electronics is presented at figure 2.4.3.1 [52]. The diagram corresponds to STM configuration. In AFM case there is no “tip voltage” and “logarithmic amplifier”. The signal is a cantilever deflection instead of tunnelling current.

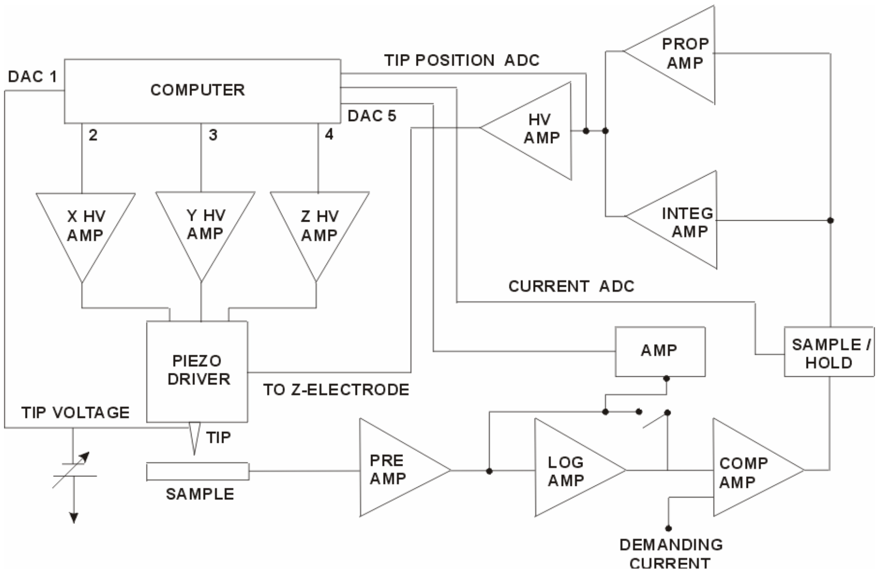

Figure 2.4.3.1. Block diagram of STM control electronics.

Tip voltage (~mV-V) may be applied by a battery or from a computer using digital to analogue converter (DAC). Tunnelling current is converted to voltage by preamplifier with gain 10^6-10^9 V/A. Logarithmic amplifier is used to lineralize exponential dependence of tunnelling current on tip-sample distance. It is important for rough surface; linear approximation of exponential dependence is valid for atomically flat surface. Measured tunnelling current is compared with reference value and resulting error signal is intensified by high voltage amplifier and applied to piezodrive Z-electrode.

2.4.4. Software

SPM is controlled from computer. The simplest program for SPM should include approach and scanning regimes. Scanning regime should make possible data receiving and processing in real time, as well as imaging of scanned region and virtual oscilloscope, which shows signal and feedback states. Scanning regime should have control parameters such as “size of scanning area”, “scanning speed”, feedback settings. Software should allow image saving and processing. The quality and development level of SPM software is very important. SPM resources are extended considerably if specific additional regimes are included, such as EFM (Electric Field Microscopy), MFM (Magnetic Force Microscopy), Kelvin Probe Microscopy and so on.

2.4.5. Probes

As mentioned above, STM has sharp metal tip as a probe. If microscope is operated at ambient conditions, tip material should be of noble metal (usually gold, platinum and platinum-iridium). Even thin oxide layer on the tip or sample surface prevents tunnelling current. Usually STM tips are prepared by user using set if simple methods, such as mechanical cutting or electrochemical etching. For very sharp surface features acquired image is influenced by the tip radius (so called “convolution”). Figure 2.4.5.1 explains this artefact. If the tip is less sharp in comparison with surface protrusions, at topography image will appear as blunt as tip itself. Influence of this artefact can be seen at Figure 3.3.5(e) in chapter 3.

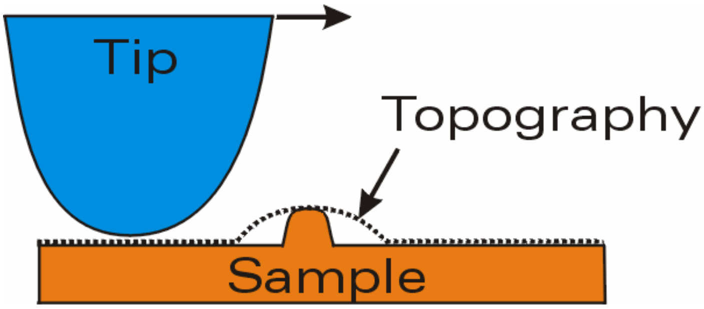

Figure 2.4.5.1. Tip convolution effect.

For AFM researchers use industrially manufactured probes. AFM cantilevers usually are made from silicon, silicon nitride, and silicon boride and optionally may be metal coated for specific applications (conductivity measurements, magnetic measurements). One or more cantilevers can be mounted on one chip. Cantilever has either I-shape (figure 2.2.1) or V-shape. Main characteristic of cantilever is the force constant and resonant frequency (last one is important only for tapping and non-contact modes). Cantilevers with small force constant (~0.01-0.1 N/m) are used for contact mode. In tapping (and noncontact) mode cantilever force constant is higher (1-100 N/m). It is important to choose proper cantilever type depending on planned application.

Chapter 3

Ge nanowire arrays inside AAO

3.1. Structure

AAO has highly ordered pore structure and can be used as template for nanowire synthesis [54, 55]. Figure 3.1.1 demonstrates idealized model of AAO pores filled with nanowires. First step in this study was to confirm that the synthesis process provides complete filling of AAO pores with germanium and nanowires were successfully formed through all length without breaking.

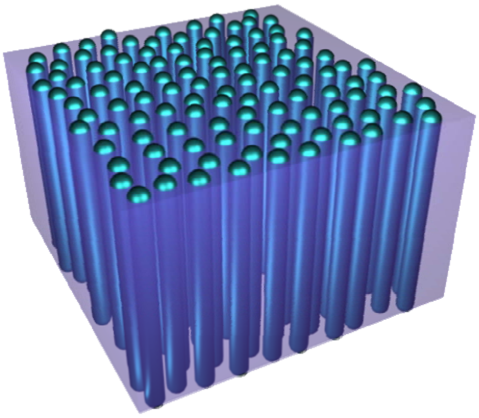

Figure 3.1.1. Idealized model of nanowire array inside AAO pores.

Porous AAO membranes with a mean pore diameter of 100 nm were purchased from *SPI supplies*. AAO membranes with a pore diameter 50 nm were produced by Dr. J. Holmes researchers group in University College Cork (Ireland) (details in [56]). Figure 3.1.2 shows AFM image of empty AAO with 50 nm pores before filling (pore density is $1.4 \cdot 10^{10}$ cm^{-2}). Ge nanowires synthesis inside both 50 and 100 nm AAO membranes (as well as nanoparticle catalyst synthesized free nanowires described in next chapter) was performed by same researchers group using a supercritical fluid (SCF) deposition technique (details in [13]).

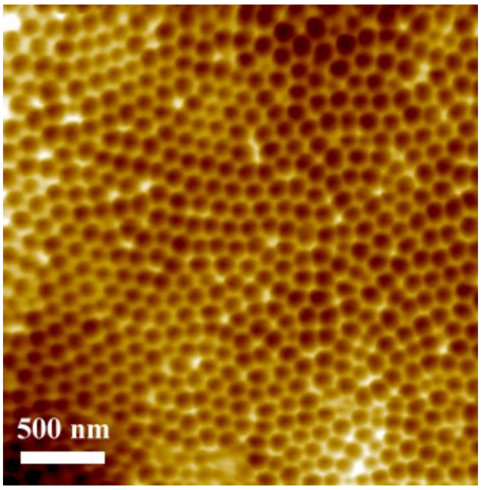

Figure 3.1.2. AFM image of empty AAO surfaces.

Figure 3.1.3(a) shows typical AFM image of the surface of a 100 nm AAO membrane after filling with Ge. Rough surface with no presence of any ordered structures was found. Most likely the surface was coated with layer of Ge film and individual nanowires were not visible on the topography measurements.

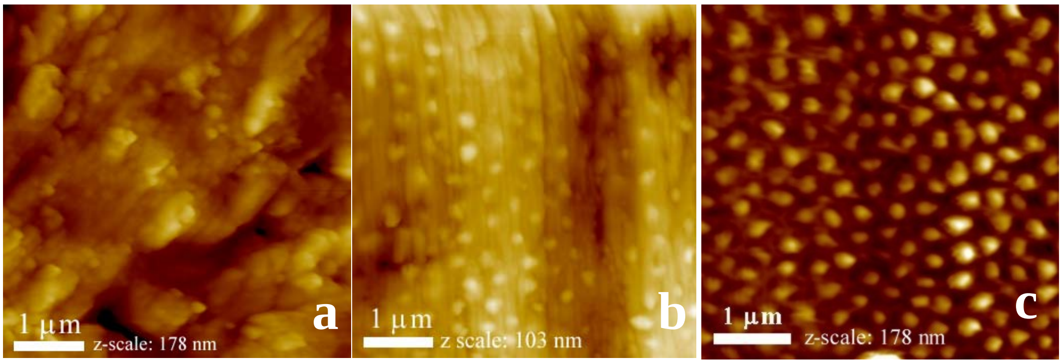

Figure 3.1.3. AFM images of AAO surfaces filled with Ge: (a) - after Ge inclusion in the pores; (b) - after mechanical polishing; ()c - after chemical etching of polished sample with 9 % H_3PO_4 .

Large numbers of well ordered protrusions extending 1-10 nm from the surface become clearly visible after sample mechanical polishing (figure 3.1.3(b)), and they are supposed to be Ge nanowires. To prove this assumption membrane surface was etched with 9 wt% H_3PO_4 for 15 minutes which selectively etch Al_2O_3. Height of protrusions was increased up to 20-50 nm (figure 3.1.3(c)), and this fact confirms our suggestion.

Moreover, individual germanium nanowires were released from the AAO membranes by dissolving the GeNW-AAO composite material with 6 M NaOH at 150 °C. The liberated nanowires were washed with distilled water and filtered. The filter was suspended in methanol and immersed in an ultrasonic bath for 20 min. The released nanowires were adsorbed onto glass slides for AFM investigation. Elongated structures 3-10 µm long (figure 2.1.4) were observed and identified as nanowires. The mean diameter of the nanowires formed within the commercial and in-house AAO templates was approximately 100 and 50 nm respectively which corresponds to the mean pore diameters of the AAO membranes used as templates.

Main property of semiconducting materials is the existence of energy gap E_g. At zero temperature semiconductors are complete insulators and with increasing temperature their conductivity increase exponentially. This provides an easy method to test whether the nanowires exhibit semiconducting properties as bulk Ge crystals.

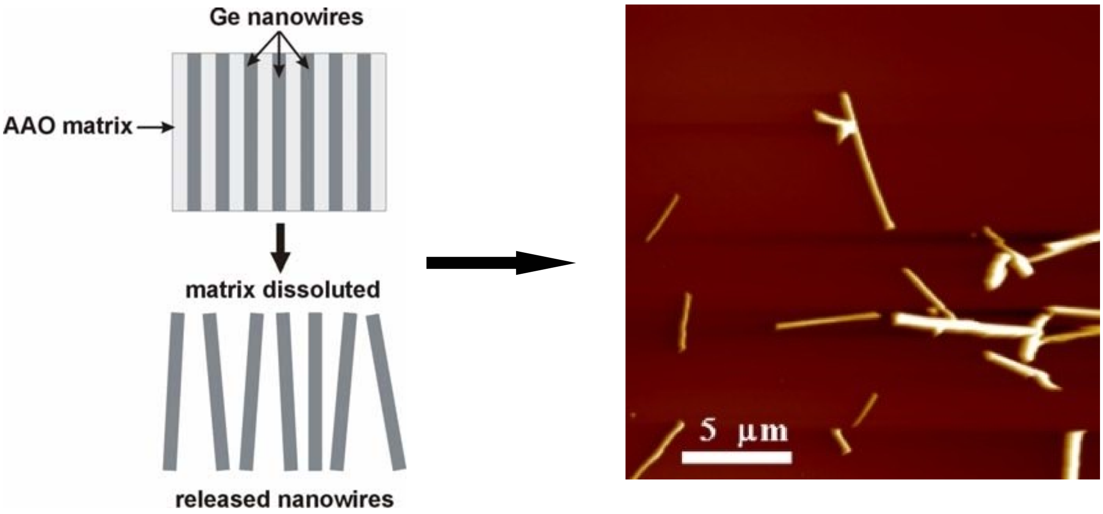

Figure 3.1.4. Schematics and AFM image of nanowires liberated from an AAO membrane.

Macrocontacts, 1 mm in diameter, were used to investigate the mean electrical properties of the Ge nanowires within the templates (more details in the section 3.3) and to determine the activation energy. For thermally activated intrinsic current carriers, which produce the current I through a nanowire, it depends on temperature T according to equation 3.1.1 [57]:

$$I = I_0 \exp\left(-E_a / 2kT\right) \qquad (3.1.1)$$

where E_a is the activation energy and k is Boltzman's constant. The activation energy of the Ge nanowires within the arrays was determined from current-temperature dependence in the temperature range between 140-300 K (figure 3.1.5). This temperature region provides information about conductivity type determined either by intrinsic or by doped charge carriers. The activation energy E_a of the Ge nanowires with a mean diameter of 100 nm and 50nm was found to be 0.61 eV and 0.58 eV respectively and both values are close to the band gap E_g value for bulk Ge at 0.66 eV [53]. From acquired data we can conclude that conductivity has intrinsic character till at least 140 K with no visible contribution of doping impurities.

Using selective surface etching and complete matrix dissolution it was shown that nanowires were formed inside AAO pores. However, the question about nanowire integrity inside AAO still remains. After Al_2O_3 dissolution the length of the released nanowires was 5-10 times shorter than membrane thickness. There are two possible ways to explain this fact.

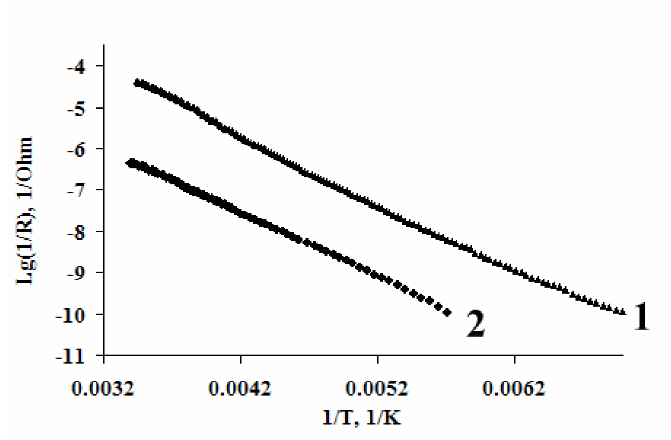

Figure 3.1.5. Conductivity dependence on temperature of Ge nanowires inside AAO membranes with a mean pore diameter of 100 nm (1) and 50 nm (2).

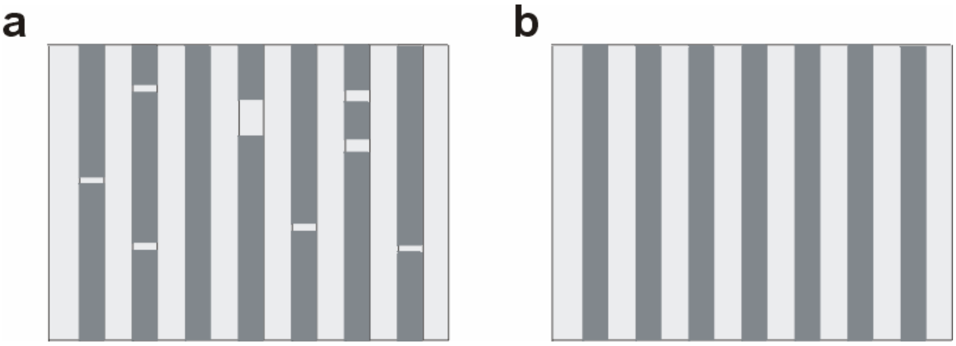

Figure 3.1.6. Schemes of possible nanowire structure inside AAO matrix. (a) – nanowires with cracks and are discontinuous through the membrane length; (b) – nanowires are continuous and without cracks.

In the first variant, the nanowires may have breaks and cracks inside membrane after synthesis already (figure 3.1.6(a)). According to the second variant, the nanowires inside AAO are continuous (figure 3.1.6(b)) and become fragmented during ultrasonic processing. It should be noted that nanowires shortening correlate with the time of ultrasonic processing. However, in order to answer this question about nanowires integrity they should be probed individually as will be shown in next section.

3.2. Single nanowires in array

Conductive probe atomic force microscope is a suitable tool for investigation of electroconductive properties of nanoobjects as well as mechanical interactions. C-AFM in contact mode was used to study electroconductivity of individual Ge nanowires incorporated into AAO membrane and to study nanowire force interactions of with C-AFM tip (figure 3.2.1). The topography, friction and conductivity images of nanowire arrays were recorded simultaneously in form of 3D maps. Third dimension is represented by color.

Images were taken at different voltages from 0 to 50 V on polished AAO membrane surface filled with Ge nanowire with diameter 100 nm. Figures 3.2.2(a) and (b) show the surface topography, figures 3.2.2c and d show current map and figures 3.2.2(e) and (f) show friction map of the same region at 15V and 50V respectively. The areas of high current density and high friction were very well correlated with the position of the nanowires on topographic image. Some nanowires which are not observed in the topographic image can be seen detected in the current and friction map (figure 3.2.3). Thus recording of friction force provides additional information about inhomogeneous phases of investigated material, which is absent in topography map.

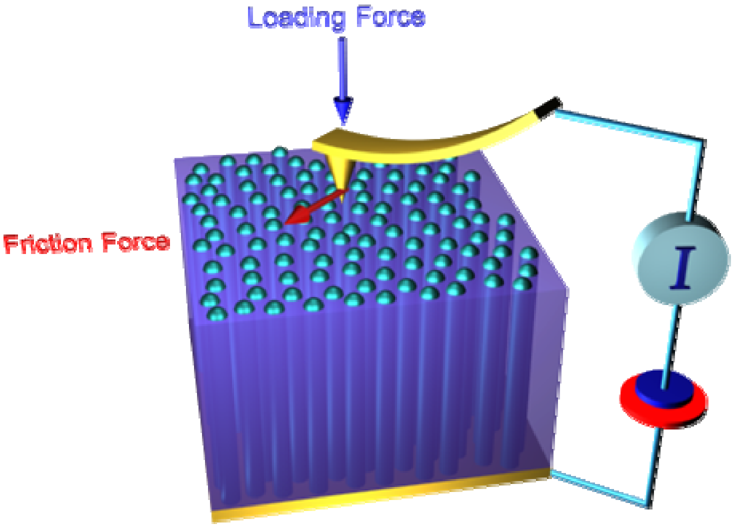

Figure 3.2.1. Scheme of C-AFM measurements on GeNW inside AAO.

From the current maps it can be concluded that nearly all of the nanowires examined were conductive throughout the entire thickness of the membrane. Current deviation through single nanowires around mean value was within ±20%. This tight current distribution indicates that nearly all of the nanowires within the array have similar conductivity characteristics. The density of Ge nanowires within the AAO membranes with mean pore diameters of 100 and 50 nm was $9 \cdot 10^8$ cm^{-2} and $1.4 \cdot 10^{10}$ cm^{-2} respectively as determined by topography and conductivity measurements.

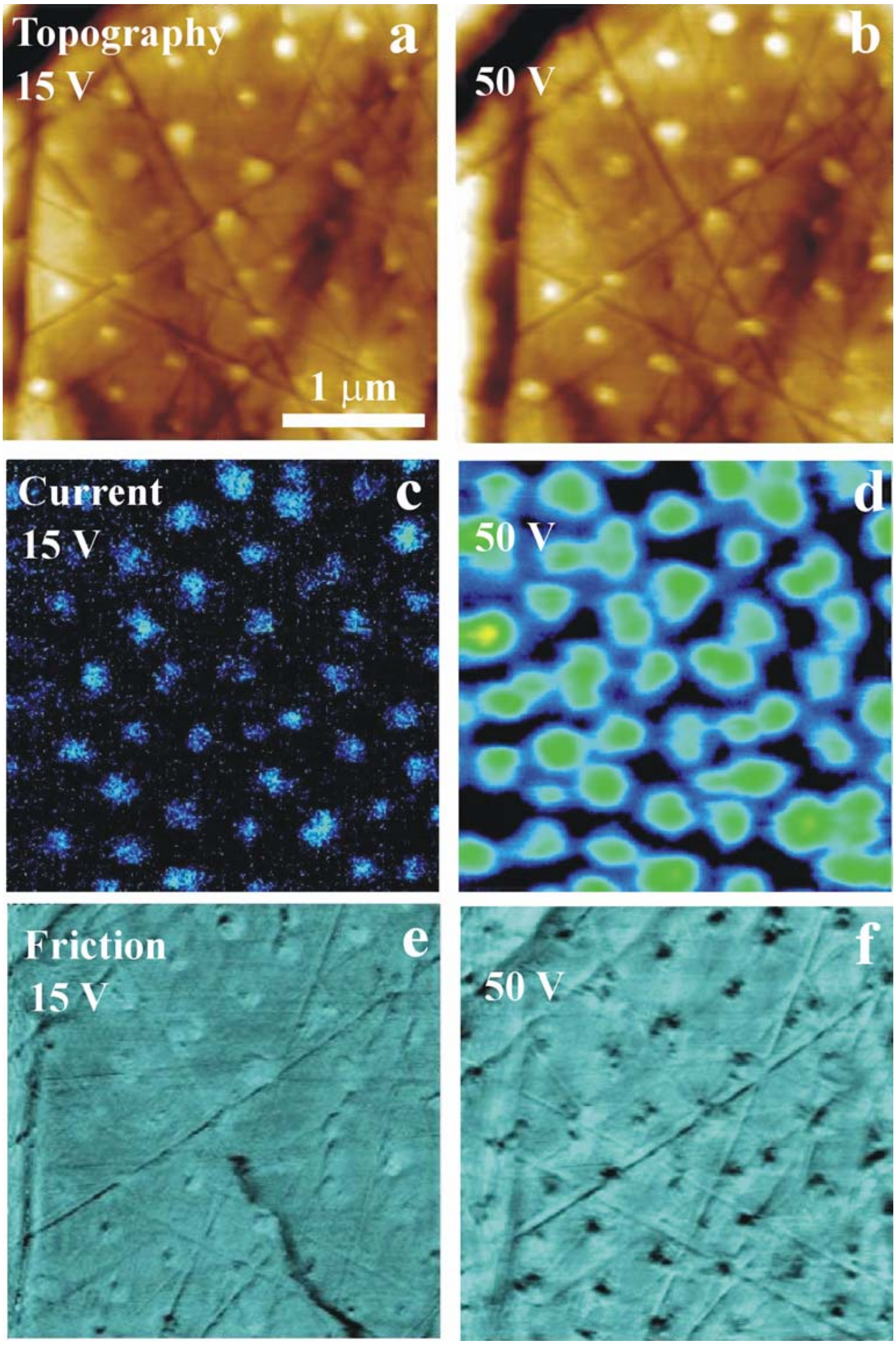

Figure 3.2.2. C-AFM images of Ge nanowire array inside AAO matrix recorded simultaneously. (a, b) - AFM topography; (c, d) – current; and (e, f) - friction force at different voltages.

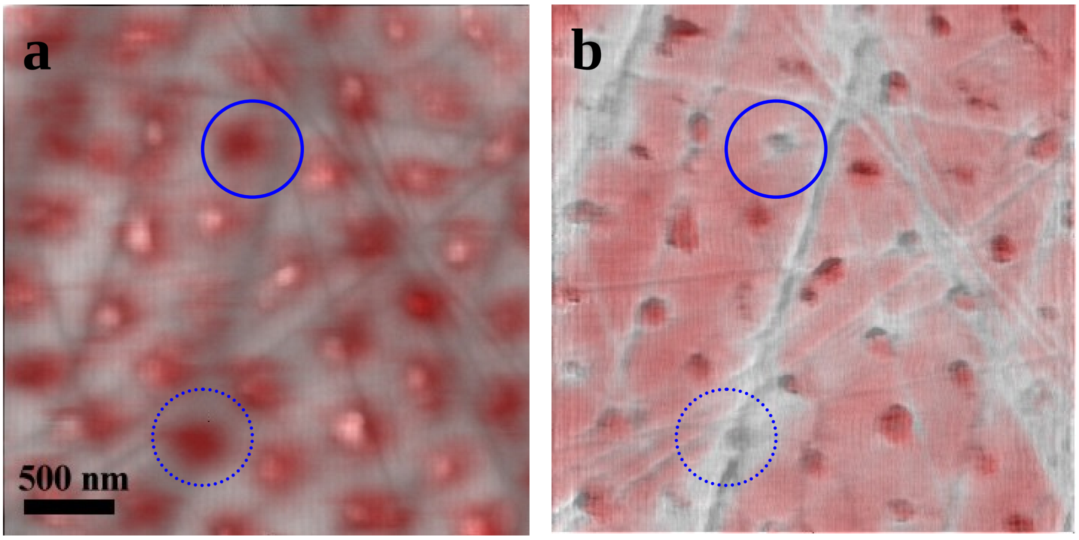

Figure 3.2.3. Combined C-AFM images. (a) - topography (grey) and current (red); (b) - friction (gray) and topography (red). Two buried (no extended) nanowires marked with solid and dashed circles for example.

During these measurements we observed also that the friction force increases then voltage raises (figure 3.2.4(a)). By applying voltage between bottom electrode and conductive AFM probe, load force also increases probably due to electrostatic interaction. At low voltages friction force on extended nanowires (figure 3.2.4(a), curve 1) is slightly higher than on buried ones (figure 3.2.4(a), curve 2), but at higher voltages friction becomes equal. Observed adhesion force increases from 9 nN at zero voltage till 41 nN at 60 V (figure 3.2.4(b)). Electrostatic force is proportional to applied voltage square, electrode shape (radius of the tip in this case), dielectric constant of the gap and inversly proportional to electrode-electrode distance.

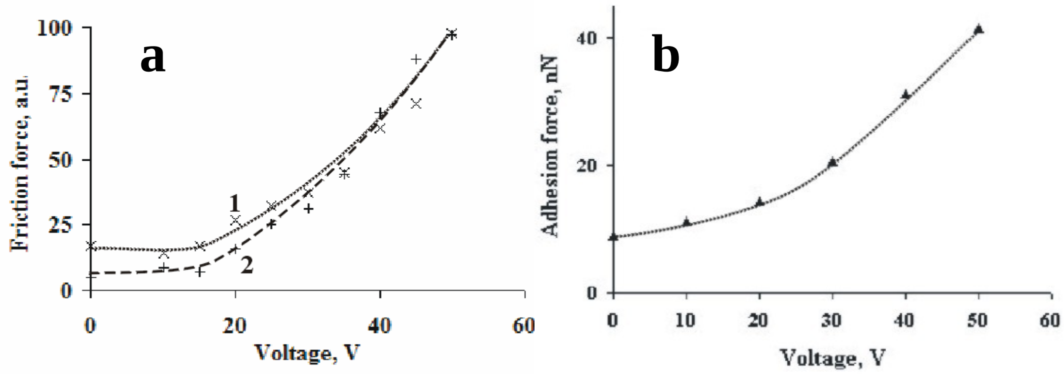

Figure 3.2.4. (a) - friction force dependence on voltage (curve 1 – measured on extended nanowires, curve 2 – on buried nanowires). (b) - adhesion force dependence on voltage.

Experimentally determined adhesion force is proportional to applied voltage square which means that additional adhesion arises as the result of electrostatic interactions between a sample and conductive AFM probe. Difference in electrostatic force between

Ge and AAO is mainly determined by dielectric constant of media and will be 1.6 times higher on Ge in comparison to AAO surface (dielectric constants 16 and 9 respectively [58]) and electrostatic force should be higher on Ge nanowire. Higher load force produce the increase of contact area. At 50 V contact area achieve 3 and 2 nm^2 on Ge and AAO surface respectively. Higher load force and contact area determines more effective increase of friction force on Ge nanowires in comparison to AAO surface.

Summarising the asquired results we can make two important conclusions. Firstly, nearly all of the semiconductor nanowires contained within the AAO substrates were conducting; each individual nanowire possessed similar electrical properties demonstrating that the nanowires are continuous and reproducible within each pore. Secondly, C-AFM with simultaneous friction force detection is powerful tool for electrical probing of individual nanowires within solid substrate.

Due to high resistance of individual nanowires it was impossible to make measurements at voltages below 10 V using our experimental setup. Measurements at lower voltage are important to exclude possible thermo ionization effect, which is possible in semiconductors in high electric field. To measure electroconductivity of nanowires at lower voltages and with no applied force, macrocontact measurements were performed.

3.3. Averaged electroconductive properties

I(V) characteristics for the polished and etched GeNW-AAO samples were measured by the macrocontact method as shown in figure 3.3.1(a). The geometry of electrode-sample assembly was approximated by equivalent scheme shown at figure 3.3.1(b). Total resistance is equal $R_{total}=R_{nw}/N$, where R_{total} – total sample resistance, R_{nw} – resistance of individual nanowire and N – number of nanowires in contact.

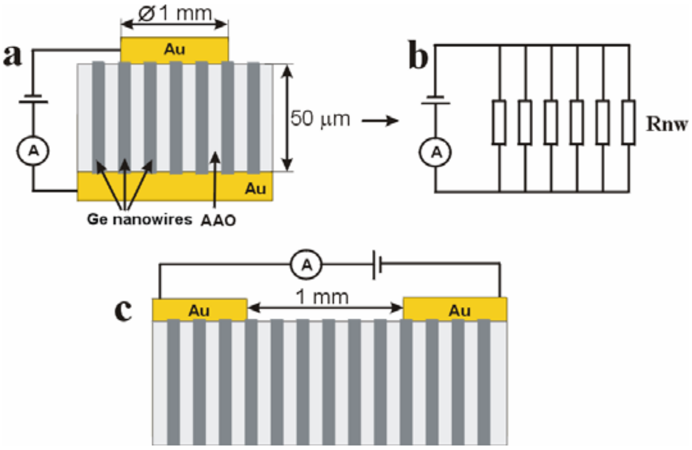

Figure 3.3.1. Representation of the macrocontact measurements setup: (a) - schematics of averaged nanowires conductivity measurement; (b) - equivalent scheme; c - schematics of surface conductivity measurement.

It was assumed that current contribution from all nanowires is equal. In reality resistance (and current) of individual nanowires deviate around some mean value and the greatest contribution into the current measured by macroelectrode comes from the less resistive nanowires. Figure 3.3.2 shows histogram of current distribution through 100 nm Ge nanowires measured by C-AFM. These data were used to compare results provided by approximate formula $R_{total}=R_{nw}/N$ and by more precise expression $1/R_{total}=1/R1_{nw}+1/R2_{nw}+\ \dots\ +1/Ri_{nw}$. Calculations show that resistance estimated using the approximate formula was 25% higher than results obtained by more precise formula. This correction is small in comparison with data variation between samples and can be neglected.

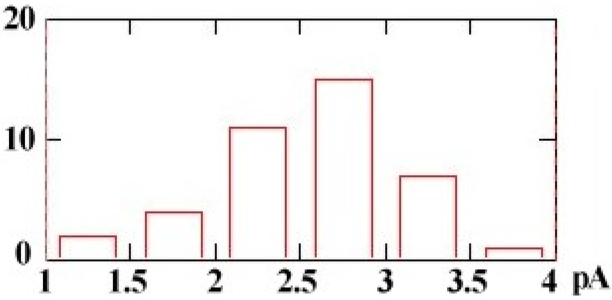

Figure 3.3.2. Histogram of current distribution through individual nanowires measured by C-AFM at voltage 20V.

The conductivity through an empty AAO matrix and surface conductivity (scheme shown at figure 3.3.1c) of the filled GeNW-AAO matrix was found to be 10^3-10^6 times lower than the conductivity through the nanowires and therefore neglected. Consequently, the I(V) data reflects the conductivity through the nanowires within the arrays.

For contacts deposited on mechanically polished samples, with no etching mostly non-linear I(V) curves were obtained for both 50 nm and 100 nm diameter nanowires (figure 3.3.3(a), curves 1 and 3). The non-linear I(V) curves in both samples may be due to a Schottky barrier between the Ge nanowire and the metal electrode or due to an insulating layer present in contact.

Meng et al recently demonstrated selective etching of AAO surface layer by 2 wt% NaOH to expose the ends of Ni nanowires [59]. It is known that Ge can be etched by NaOH also. That is why we used 9 wt% H_3PO_4 instead of NaOH for selective chemical etching of the AAO top layer around the nanowires to improve its contact to metal electrode. It was noted that the etching rate for 50 and 100 nm AAO membrane is different. Etching times were chosen 15-90 min for 100 nm GeNW-AAO and 3-10 min for 50 nm GeNW-AAO arrays at room temperature. At these etching conditions the only thin (≤100nm) surface layer of Al_2O_3 is removed and nanowire ends expose above the surface of AAO membrane. This allows enlarging of nanowire / metal film electrode contact area. Conductivity for the 50 nm case improves approximately 10 times (figure 3.3.3(a), curves 1 and 2) while the conductivity of the 100 nm diameter GeNW-AAO samples improves only approximately 1.5 times (figure 3.3.3(a), curves 3 and 4) in comparison to mechanically polished samples. It means that chemical treatment is much more useful for 50 nm samples in comparison with 100 nm ones for contact improvement.

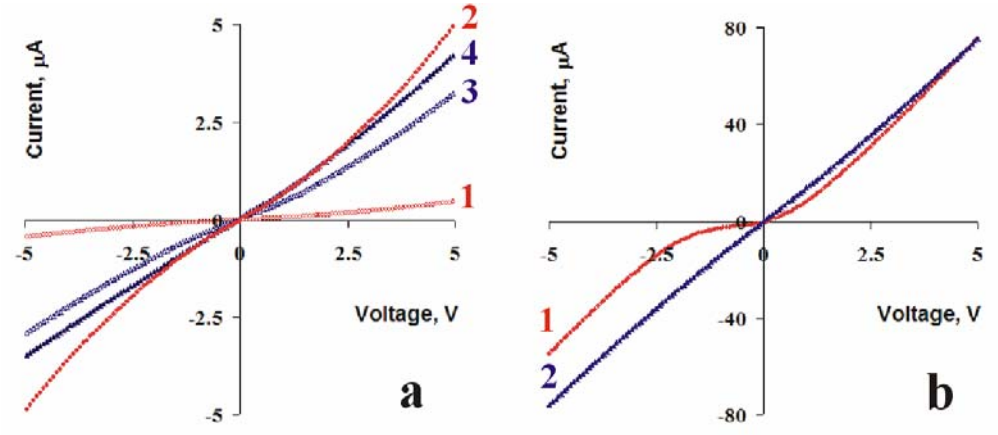

Figure 3.3.3. I(V) data for Ge nanowire arrays. (a) - comparison of etched and nonetched samples: curve 1 - 50 nm sample without etching, 2 – 3 min etched; 3 – 100 nm nonetched sample, 4 – 15 min etched. (b) – best achieved results: 1 – 50 nm sample etched 10 min, 2 – 100 nm sample etched 90 min.

It was estimated that the contact surface in case of 50 nm nanowires (surface density $1.4 \cdot 10^{10}$ cm^{-2}) increase app. 8 times more in comparison with 100 nm nanowires (surface density $9 \cdot 10^{8}$ cm^{-2}) if same surface layer of Al_2O_3 (100 nm) was removed by chemical etching. It is in good agreement with obtained results, then resistance of 50 nm nanowire array was decreased 6.7 times more in comparison with 100 nm. Further etching is useless because highly nonuniform and deep cracks appear (figure 3.3.4).

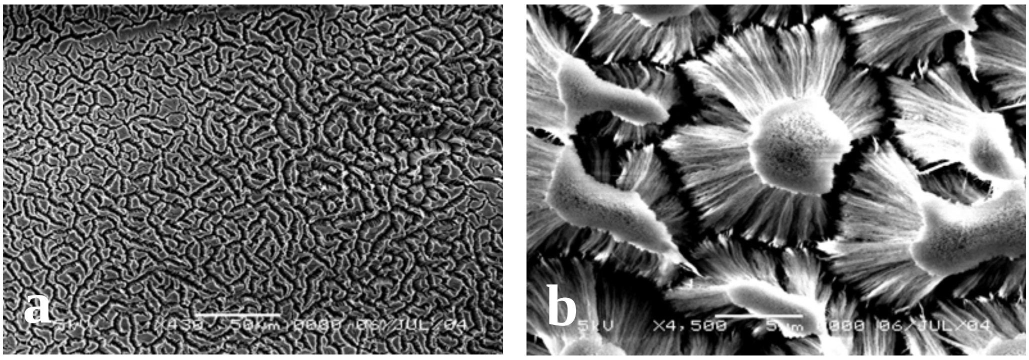

Figure 3.3.4. SEM images of 50 nm GeNW-AAO membrane surface modification at long etching (10 minutes etching in 18% HCl). (a) - scale bar – 50 µm, (b) – scale bar 5 µm. (courtesy of Brian Daly, University-College Cork).

The I(V) characteristics of the 100 nm diameter Ge nanowires became almost linear and displayed good ohmic contact characteristics after chemical etching (figure 3.3.3(a) - curves 4; (b) - curve 2). This change implies that the nonlinearity observed with the non-etched samples is due to the presence of an insulator layer, i.e. AAO, between the nanowires and the metal electrode. A degree of nonlinear behavior was however still observed for the 50 nm diameter nanowires after polishing and etching (figure 3.3.3(a) - curve 2; (b) – curve 1), which may imply that the AAO layer around the 50 nm nanowire was not completely removed after etching.

In the ideal case H_3PO_4 should uniformly remove the AAO layer around the nanowire as shown in figure 3.3.5(a) and (b).

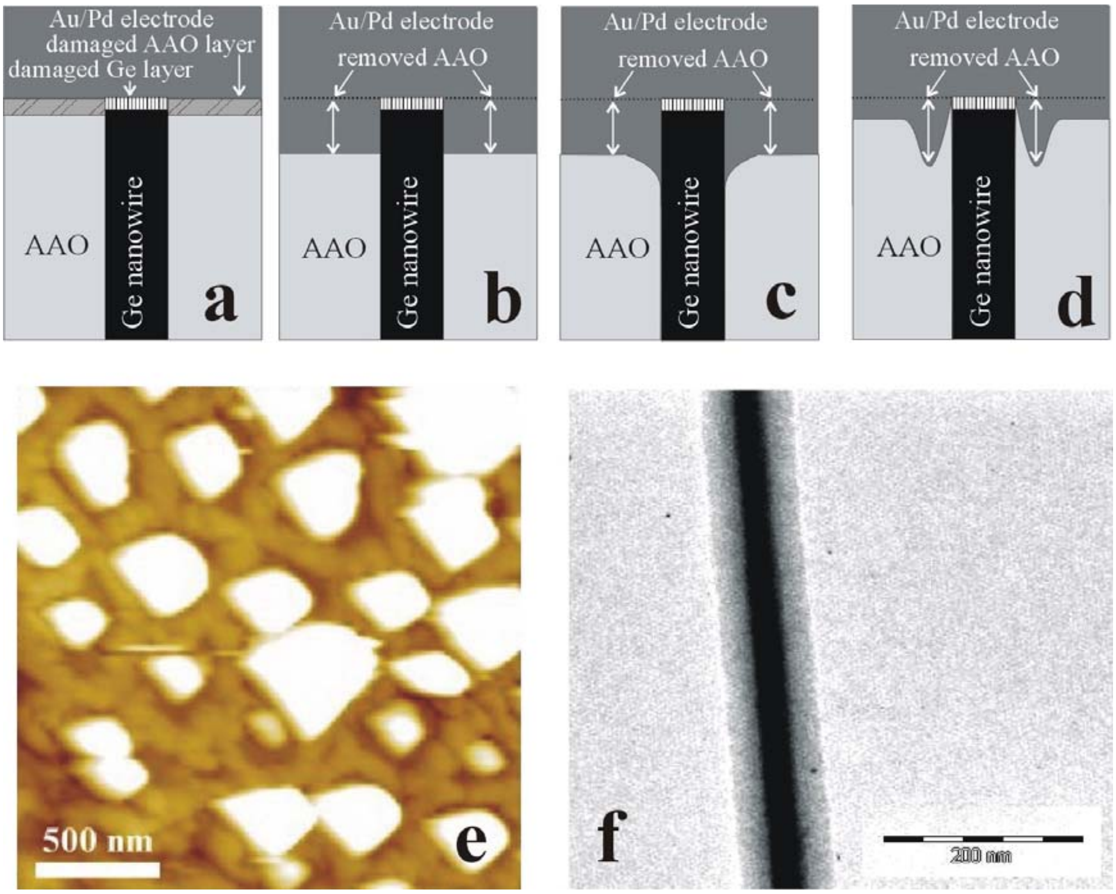

Figure 3.3.5. Schematics of: (a) - contact on polished surface before etching; (b) - assuming homogenous removal of the AAO matrix during surface etching; (c) - assuming more effective AAO matrix etching in close proximity to the nanowire for 100 nm diameter GeNW-AAO samples; (d) - assuming more effective etching away from nanowire for the 50 nm diameter GeNW-AAO samples; (e) - AFM topography surface image of 100 nm nanowire array 15 min etched in 9 % H_3PO_4 (note that high protruding nanowires appear thick due to tip convolution effect); (f) - TEM image of 50 nm Ge-NW released from AAO (courtesy of Jana Andjane, Institute of Chemical Physics).

For 100 nm GeNW-AAO samples, the etching occurs more efficiently around the edge of the nanowire as shown in AFM image (Figure 3.3.5(e)). A schematic of this situation is shown in Figure 3.3.5(c). Dark areas around the nanowires (figure 3.3.5(e)) correspond to effective removal of AAO material in comparison to areas between the nanowires. For the 50 nm GeNW-AAO samples, the presence of nonlinear I(V) characteristics (figure 3.3.3(c), curve 2) even after gradual etching of the surface may be due to poorer etching of the alumina in close proximity to the nanowires (figure 3.3.5). Probably, aluminum oxide around nanowires may be chemically modified at high temperatures (500 ° C). This hypothesis was confirmed by TEM study of 50 nm GeNW released from AAO (figure 3.3.5(f)). Nanowires (nanowire diameter equal to AAO pore diameter is about 50 nm) were coated with AAO layer (thickness about 30 nm) which was not removed even at harsh etching conditions (treatment with 6 M NaOH).

The resistivity calculated for a single nanowire, based on a mean value obtained for a group of nanowires, was between 60-750 Ωm and 110-2300 Ωm for nanowires with mean diameters of 100 nm and 50 nm respectively. Higher resistivity of 50 nm nanowires in comparison with one of 100 nm may be explained by size effect. Surface to volume ratio is higher for thinner nanowires, and hence higher probability for electron to be scattered at surface imperfections.

Figure 3.3.6 illustrates a comparison between the C-AFM and macrocontact measurements for GeNW-AAO samples. At higher voltages (50 V) the resistivities decrease 2-3 times for both C-AFM and macrocontact measurements. The reason for the lower resistivity at higher voltages is possibly due to thermoelectric ionization [60]. The change in resistance through the nanowires as a function of applied voltage is almost identical for both the macrocontact and C-AFM measurements (figure 3.3.6).

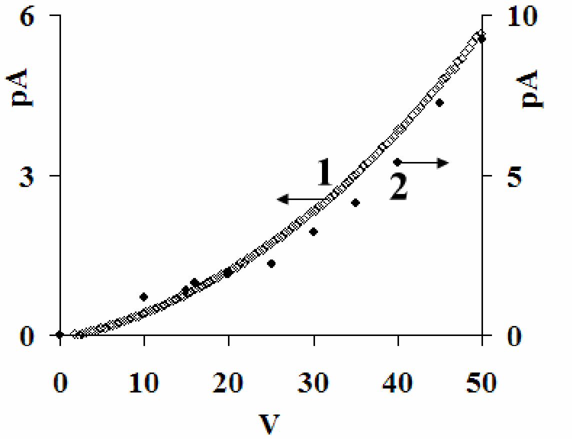

Figure 3.3.6. Dependence on the current vs. voltage dependence through an individual 100 nm Ge nanowire measured by (1) macrocontact and (2) C-AFM.

Resistivity values for a single nanowire for both systems are approximately the same despite the contact area of single nanowire with the macrocontacts being 3 orders of magnitude larger, 8000 nm^2 for the 100 nm diameter nanowires and 2000 nm^2 for the 50 nm diameter nanowires, than the contact area with C-AFM, i.e. 2-4 nm^2. This result suggests that for the polished samples, both the C-AFM and macrocontact methods are inherently suitable for measuring the electrical properties of such the nanowire arrays.

It should be noted also that there may be differences in the nature of the association between the nanowire and the metal contact for the macrocontact and C-AFM methods. In C-AFM measurements a force is applied between the AFM tip and the surface which can improve the quality of the contact. In addition, the AFM tip can penetrate into the AAO pores and contact with the buried nanowires. In macrocontact case, the metal is deposited on the top of the GeNW-AAO surface and some buried nanowires may be not contacted to the electrode.

Resistivity values for our nanowires encapsulated inside AAO templates are significantly higher than the resistivity of bulk Ge (0.66 Ωm). For the Ge nanowires incorporated within the AAO, nanowire resistivities would be expected to be higher than bulk Ge due to much higher surface area, which breaks symmetry of perfect crystal and hence increase electron scattering probability [2]. Our Ge nanowires grown inside of AAO show also higher resistivities than individual Ge nanowires, as was reported in the literature, e.g. $1.4\cdot10^{-4}$-$3\cdot10^{-1}$ Ωm [61] for Ge nanowires grown on gold nanoparticles by a VLS mechanism and 10^{-3}-10^{-1} Ωm [62] for Ge nanowires grown from gold nanoparticle-seeded supercritical fluid-liquid-solid (SFLS) method using a continuous flow reactor. In the next chapter we will also compare electroconductive properties of template synthesized nanowires and nanoparticle-seeded nanowires synthesized by the same SCF method. It should be noted that nanowires grown on gold nanoparticles are doped in contrast to our nanowires. To our knowledge there is no data on intrinsic (undoped) Ge nanowires.

3.4. Averaged photoconductive properties

It is shown in previous sections that germanium nanowires are successfully synthesized inside pores of 50 and 100 nm AAO membranes. Nanowires are electroconductive and exhibit intrinsic conductivity. In this section photoconductive properties of Ge nanowire arrays are described. Recently nanostructures of indirect band gap semiconductors such as silicon and germanium attracted scientific interest because of their potential applications in nanophotonics and nanoelectronics, but no studies on photoconductivity of semiconducting nanowires inside AAO has been reported. Main aims of this topic were to test whether the nanowires exhibit photoconductivity and check if any AAO substrate effects are present. Figure 3.4.1 illustrates a schematic of the photoconductivity measurement setup.

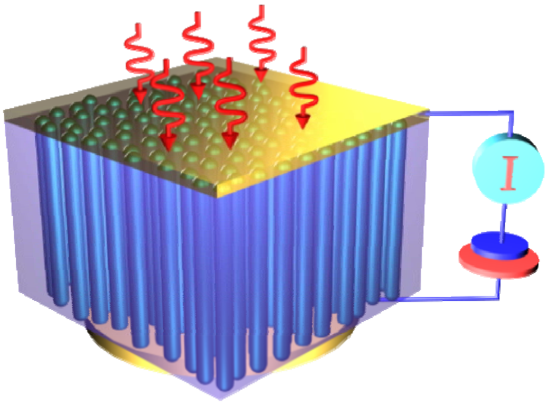

Figure 3.4.1. Schematic of photoconductivity measurements on a Ge nanowire array. The Ge filled AAO membrane was coated with an ITO or semitransparent Au electrode from the upper side and with a 100 nm thick 1 mm in diameter Au electrode from the lower side. The sample was illuminated with a multyline laser light of wavelength in range of 457-514 nm through the transparent electrode. Bias voltage was applied between the top and bottom electrodes to measure the dark current and photocurrent.

In these experiments Indium Tin Oxide (ITO) was employed to measure the photoconductivity properties of the GeNW-AAO and compared with a semitransparent gold electrode to exclude material specific contact phenomena which may be caused by n-type of ITO material. Prior to optical measurements, the contact was optimized using chemical etching of the membrane surface with phosphoric acid for both the ITO coated (ITO-GeNW-AAO) and semitransparent gold (Au-GeNW-AAO) samples following by etching procedure described in previous section. Regardless of contact optimization it was found that the resistivity of the ITO coated samples was 4-8 times higher than samples coated with Au (Figure 3.4.2(a) and (b), Table 3.4.1) for both 50 and 100 nm nanowire arrays. This can be explained by oxidation of Ge nanowires during ITO coating in an atmosphere, which contains O_2.

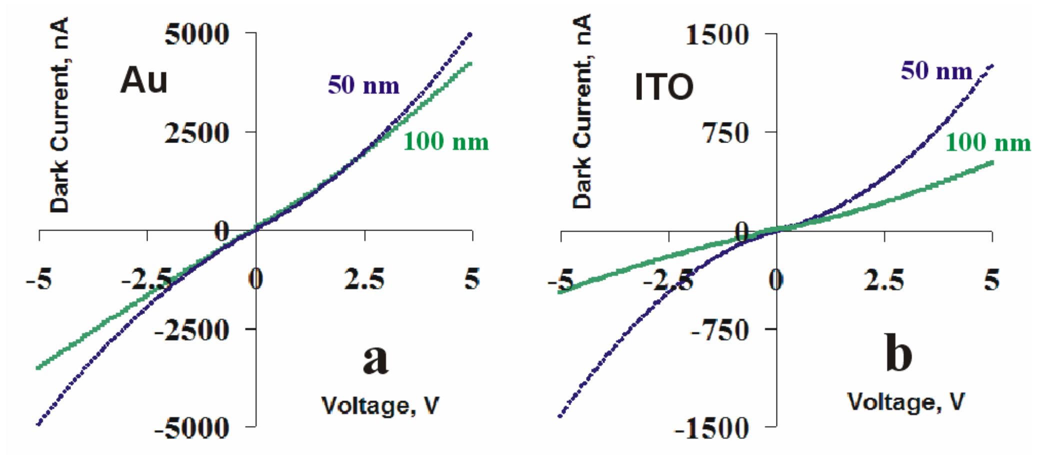

Figure 3.4.2. (a) - dark current $I_d(V)$ curves for samples with semitransparent Au electrodes; (b) - for ITO electrodes.

Table 3.4.1. Resistance of a single nanowire estimated for various GeNW-AAO samples.

Sample	Resistance (Ω) ITO Contact	Resistance (Ω) Semitransparent Au Contact
50 nm GeNW-AAO	$2.3*10^{14}$	$6*10^{13}$
100 nm GeNW-AAO	$6.4*10^{13}$	$8.4*10^{12}$

A significant increase in the current was observed for the GeNW-AAO samples during illumination with an Ar laser, intensity of 800 mW cm^{-2} and wavelength range between 457-514 nm, for both the ITO and semitransparent top Au electrodes. No effect was detected at the same conditions in empty AAO membranes, i.e. those not loaded with Ge nanowires in the pores. The photocurrent dynamics in the NW-AAO arrays were measured using short (0.5 ms) and long (1 s) illumination pulses as shown in figures 3.4.3, 3.4.6 respectively. The samples display exponential growth and decay kinetics with the characteristic time constants (τ_i) ranging from sub milliseconds to seconds. Mathematically the time dependence of current can be expressed as [63]:

$$I_{total}(t) = I_0 \pm \sum_i C_i \cdot \exp(-t/\tau_i) \qquad (3.4.1)$$

where I_{total} is the current detected after a time t, I_0 is equal to steady current at given illumination intensity (damping of photocurrent, when illumination is switched off) or dark current (starting of photocurrent, when illumination is switched on), C_i is a numerical coefficient, which describe the contribution of each photoinduced process, and τ_i is the current change time constant.

In simple case, absorbed photons generate electron-hole pairs in the semiconducting crystal. The increase of the charge carrier concentration consequently causes the increase of electroconductivity. Photogenerated charge carriers can also recombine. Competition of generation and recombination processes results in steady concentration of photogenerated charge carriers, then speed of generation and recombination processes are equal. Photoconductivity damping kinetics, characterised by time constant τ, is determined by electron-hole recombination speed then illumination is switched off. In the real crystals photoconductivity damping is more complicated [64].

To estimate the kinetics on the millisecond timescale individual short (0.5 ms) pulses were used (figure 3.4.3). Two kinetic components (τ_1 and τ_2) were determined by fitting the experimental data to exponent (figure 3.4.3b and table 3.4.2.)

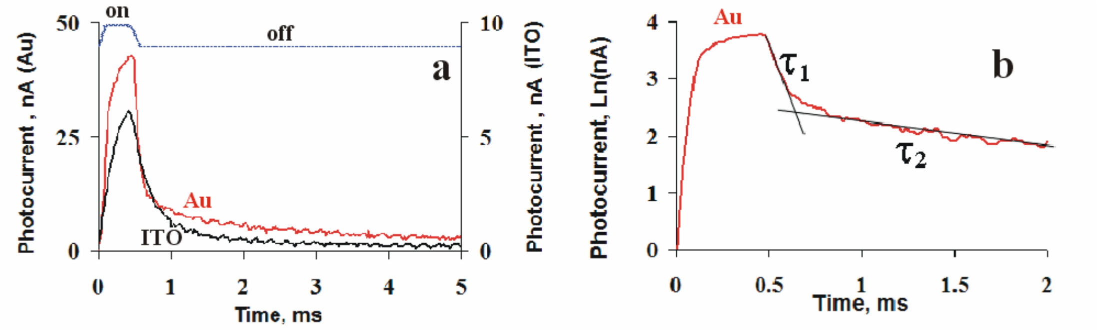

Figure 3.4.3. (a) - current response during 0.5 ms illumination by laser intensity 800 mW cm^{-2} for 100 nm nanowires with Au and ITO electrodes (kinetics of 50 nm nanowires are similar); (b) – photocurrent damping kinetics for same sample with Au electrode.

The decay kinetic component (τ_1) appear in experiment as fast as operation time (10^{-5} s) of equipment used. Real values of τ_1 were obviously obscured by equipment speed and were less than 10^{-5} s. It may be close to the charge carrier life time reported in literature for polycrystalline Ge was 3 μs [65] and 1-50 μs [66]. Polycrystalline Ge is good analogy to nanowires because of high amount of grain boundary associated defects.

The second photokinetic process shows time constants (τ_2) in the range of 10^{-3} s and summarized in table 3.4.2. We attribute it also to electron – hole recombination in Ge. In this process electron-hole pairs can be generated by photo luminescent light primarily adsorbed by AAO matrix and emitted according to the luminescence kinetic

(τ_{lum}). Photoluminescence decay time constant was found to be in range 0.8-2 ms for both 50 and 100 nm Ge nanowires inside AAO (figure 3.4.4).

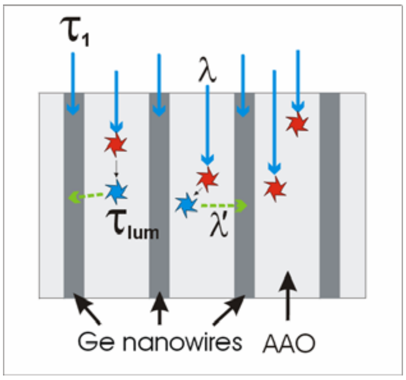

Figure 3.4.4. Scheme of light absorption in GeNW-AAO system. Laser photons (blue arrows) absorbed by Ge nanowires create electron-hole pairs (recombination time constant τ_1). Photons may also be absorbed by AAO and they excite photoluminescence centres (red stars), which relax to the normal state (time constant τ_{lum}) (blue stars) and emit accumulated energy as luminescence photons (dashed green arrows) with longer wavelength $\lambda' > \lambda$. Then photoluminescent light may be absorbed by Ge nanowires and impact into photocurrent with time constant $\tau_2 \sim \tau_{lum}$.

In case of 50 nm pore AAO photoluminescence intensity was about an order of magnitude more intensive than 100 nm AAO (Figure 3.4.5). Elimination of AAO photoluminescence is essential for creation fast optoelectronic devices based on arrays of semiconducting nanowires inside AAO.

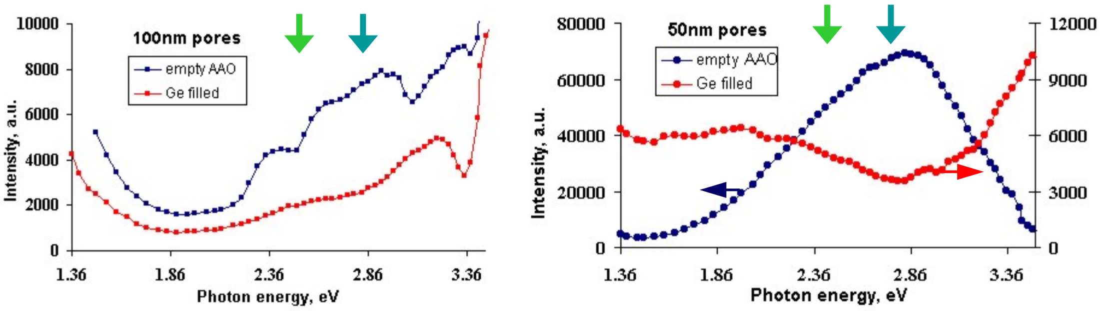

Figure 3.4.5. (a) - photoluminescence of empty and Ge filled 100 nm AAO membranes. (b) - photoluminescence of empty and Ge filled 50 nm AAO membranes. Blue and green arrows indicate laser wavelength used in photoconductivity experiments.

One more component with time constant (τ_3) about 0.5-4 s was determined after illumination of the nanowire-AAO samples with a 1 s long laser pulse (figure 3.4.6 and table 3.4.2). We associate the kinetic component (τ_3) with thermo generated current caused by sample heating by laser illumination. Sample heating was directly measured using copper-constantan thermocouple attached on the back side of GeNW-AAO membrane (figure 3.4.7(b)). At short pulses (0.5 ms) sample temperature rise is negligible (10^{-3} K). At long pulses the temperature rises (decrease) with time linearly as $T(t) \sim t/\tau_{th}$ at initial time interval and stabilizes after about 10 s as it shown in figure 3.4.7(a).

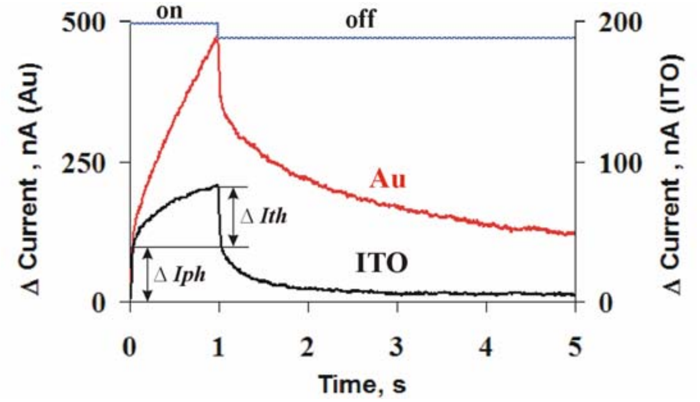

Figure 3.4.6. Current change during 1 s pulse illumination and after for 50 nm Ge nanowire sample for Au and ITO electrodes (kinetics of 100 nm nanowires is similar). Dark current is set to zero here. Impacts of photo- generated and thermo-generated currents are shown as ΔI_{ph} and ΔI_{th}.

Values of current change kinetics (τ_3~0.5-4 s) are very close to heating kinetics (τ_{th}~0.5-1 s), which allow us to identify τ_3 with τ_{th}. Current through Ge nanowires inside AAO depend on temperature as I ~ exp($-E_a/kT$) (figure 3.4.7(c)).

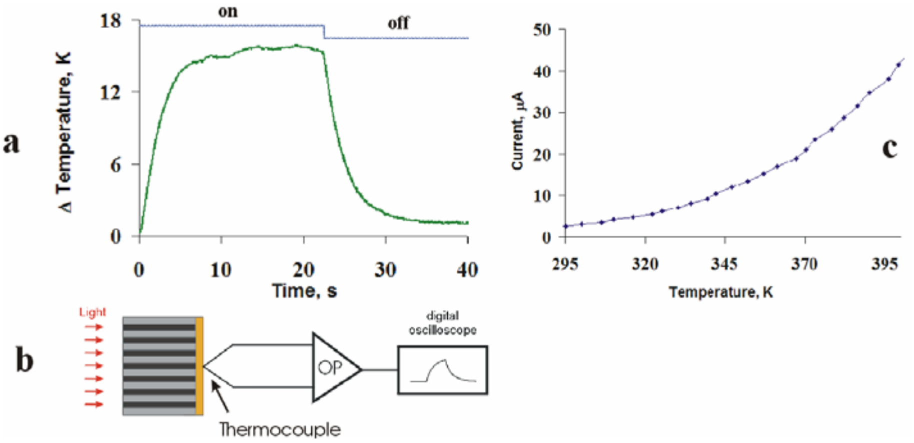

Figure 3.4.7. (a) - sample heating / cooling dynamics at illumination by laser intensity 800 mW cm^{-2} for 100 nm Ge nanowires (50 nm sample have very similar dynamic). (b) – measurement setup. (c) - exponential increase of current on temperature.

Thus linear growth of sample temperature will cause exponential increase of current. We can separate contributions of temperature caused current increase ΔI_{th} and photo induced current increase ΔI_{ph} as it shown at figure 3.4.6, taking into account that photocurrent kinetics (τ_1 and τ_2) is about 1000 times faster than thermo generated current kinetic (τ_{th} or τ_3). Note, that ΔI_{th} impact into current is higher relative to ΔI_{ph} in case of Au electrode in comparison to ITO electrode. We can explain it by taking into account the fact what Au electrode converts more light to heat than ITO electrode and sample heating in first case is higher.

Table 3.4.2. Comparative table of photoresponse (τ_2) and heating time constants (τ_3) for GeNW-AAO samples.

Nanowire diameter	Electrode	τ_2 (ms)		τ_3 (s)	
		increase	decrease	increase	decrease
50 nm	**ITO**	0.4-0.5	1-3	2-3	0.5-4
50 nm	**25 nm Au**	0.4-4	3-7	0.5-1	2-2.5
100 nm	**ITO**	0.25-0.5	0.8-2	1.5-5	1-1.4
100 nm	**25 nm Au**	0.4-0.8	0.5-4	1-1.5	1.7

Figures 3.4.8(a) and (b) show the photocurrent (I_{ph}) as a function of applied voltage for the samples with ITO and semitransparent Au electrodes respectively for 50 and 100 nm Ge nanowire arrays. $I_{ph}(V)$ exhibit almost linear growth with applied voltage for both samples and both contacts.

The photo current / dark current ratio (I_{ph}/I_d) was typically 10-25 % and 3-5 % for the ITO-nanowire and Au-nanowire contacts respectively for both chemically etched and non-etched samples. The difference in the I_{ph}/I_d ratios is probably due to the lower transparency of the top Au-contact compared to the ITO electrode. We have measured that light intensity decreases by 50 % after passing through Au thin film of the same thickness (25 nm) as was used to coat our samples. As ITO is almost completely transparent, the loss of light is negligible.

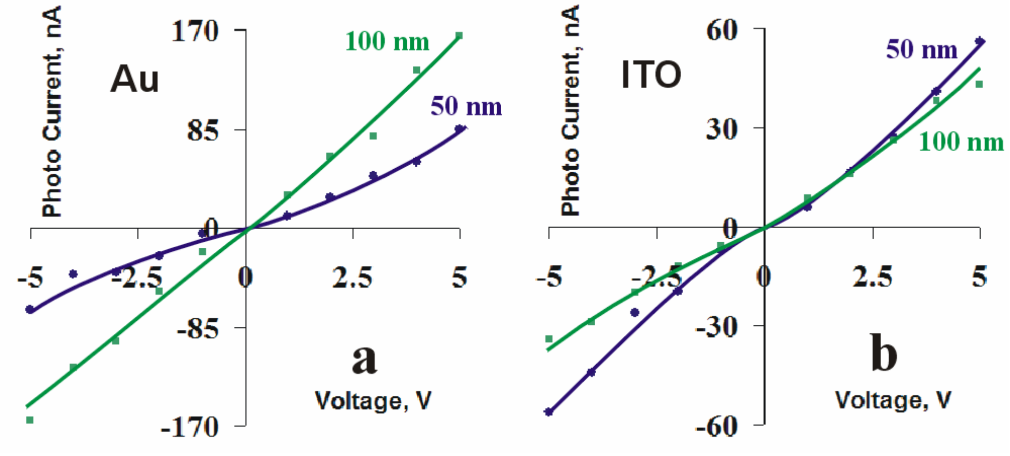

Figure 3.4.8. (a) – photocurrent-voltage curves for samples with ITO electrodes ($I_{ph}=I_{total}-I_{dark}$); (b) - semitransparent Au electrodes detected after 50 ms of laser illumination of intensity 800 mW cm^{-2}.

Thus, taking into account the low intensity of light transmitted through the Au electrode, the Au and ITO coated samples show practically the same I_{ph}/I_d ratios. Comparing Au and ITO electrodes, we would note better contact of Au electrode with nanowires and consequently higher currents. However, losses of light intensity if Au electrode used are significant.

Bearing in mind the photocurrents shown in figures 3.4.8a and b, we estimate that the photocurrent in a single Ge nanowire with Au electrode, at a *bias* of 5 V and illumination power of 800 mW cm^{-2}, is in the range of 30 fA for the 100 nm nanowires and approximately 3 fA for the 50 nm nanowires, respectively. $I_{ph}(V)$ curves also show approximately linear growth of photo current with the bias voltage increase (figure 3.4.9(a)), thus one can obtain higher current at increased voltages. Photocurrent is 10 times higher at 50 V in comparison to 5 V. This indicates that the Ge nanowires within the AAO templates demonstrate a sufficient photoinduced current, and it means that this material can be used for creation of high resolution devices. Proposal of ultra high resolution photosensitive matrix based on nanowire array inside AAO is described in chapter 6.

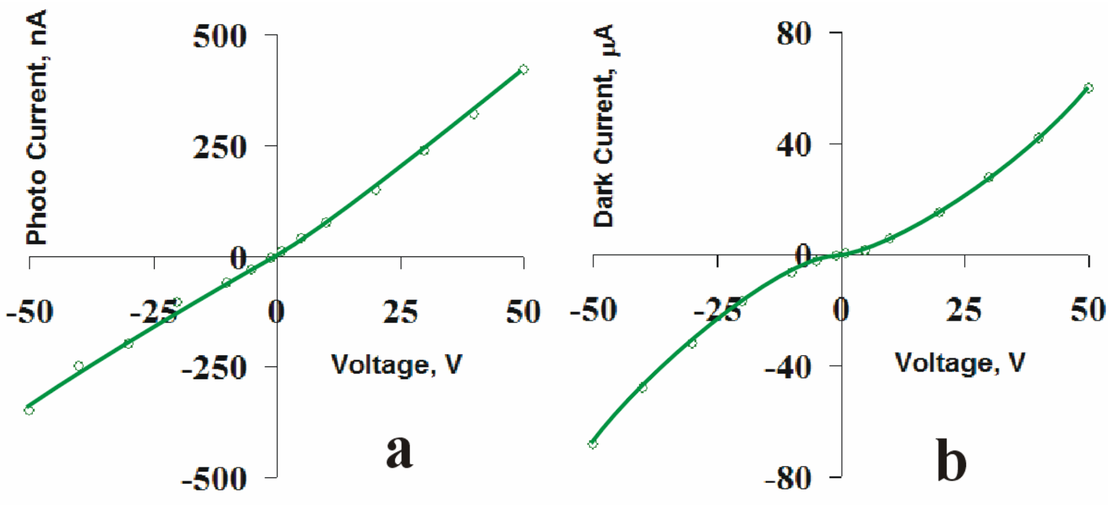

Figure 3.4.9. (a) - photocurrent $I_{ph}(V)$ curve at high voltages for 100 nm sample with semitransparent Au electrode detected after 0.5 ms of laser illumination of intensity 800 mW cm^{-2}. (b) - corresponding dark current for same sample.

CHAPTER 4

NANOPARTICLE CATALYST SYNTHESIZED FREE GE AND SI NANOWIRES

In this chapter were used nanowires grown on Au metal tips from Au nanoparticles, which were present on tips, using SCF method. The same method was used for synthesis of nanowires inside AAO template. The main aim of this study was to compare properties of nanowires synthesized with these two methods. In particular, structure, electroconductive properties and force interactions of free nanowires are described here. Acquired information was analyzed and used to elaborate and demonstrate principles of a nanoelectromechanical device as well as its 3D array (chapter 6). At the end of this chapter some advantages of nanowire template synthesis are summarized.

4.1. Structure

Transmission electron microscopy (TEM) is a unique technique which reveals internal structure of nanoobjects and in combination with energy disperse X-ray spectroscopy (EDX) it allows to probe elemental analysis with ultra high spatial resolution. Figure 4.1.1 show images of typical Si nanowire. Nanowires have diameter in interval 40-90 nm and visible length 2-10 μm. A small Au nanoparticle was usually visible at the very end of nanowire. Gold particle acts as a catalyst and nucleate growth of nanowires. It is well known VLS mechanism there nanowire grow from Au-Si or Au-Ge eutectics [67]. It is natural that during growth at high temperatures nanowires become Au doped as further is shown. Figure 4.1.1 presents results of EDX elemental analysis of typical Si nanowire. Nanowire body consist of Si with negligible traces of oxygen (due to nanowire oxidation at ambient conditions), carbon (nanowires were synthesized in CO_2 atmosphere), titanium and copper, which were used as TEM holder material. The very end of nanowire consists of gold. Ge nanowires have very similar structure.

4.2. Electroconductive Properties

Electroconductivity of the nanowires was studied using Scanning Probe Microscope compatible with transmission electron microscope (TEM-SPM). Si nanowires typically displayed linear I(V) behavior as shown in figure 4.2.2(a), and was independent of the point of contact between the nanowire and the gold electrode.

The resistance of the Si nanowires did not vary significantly with contact area (same as in previous chapter) when the contact diameter was changed between 4 and 55 nm resulting in resistances between 15 and 45 MΩ without correlation to contact area. Although the contact resistances cannot be adequately determined through a simple two-point contact, the resistivities of the Si nanowires can be estimated to be of the order of 10^{-2} Ω m. The relatively low resistivities for Si nanowires are indicative of a highly doped nanowire with an impurity concentration of approximately 10^{16} cm^{-3}. Typical I(V) curve of Ge nanowires (40–150 nm in diameter) is shown in figure 4.2.2(b).

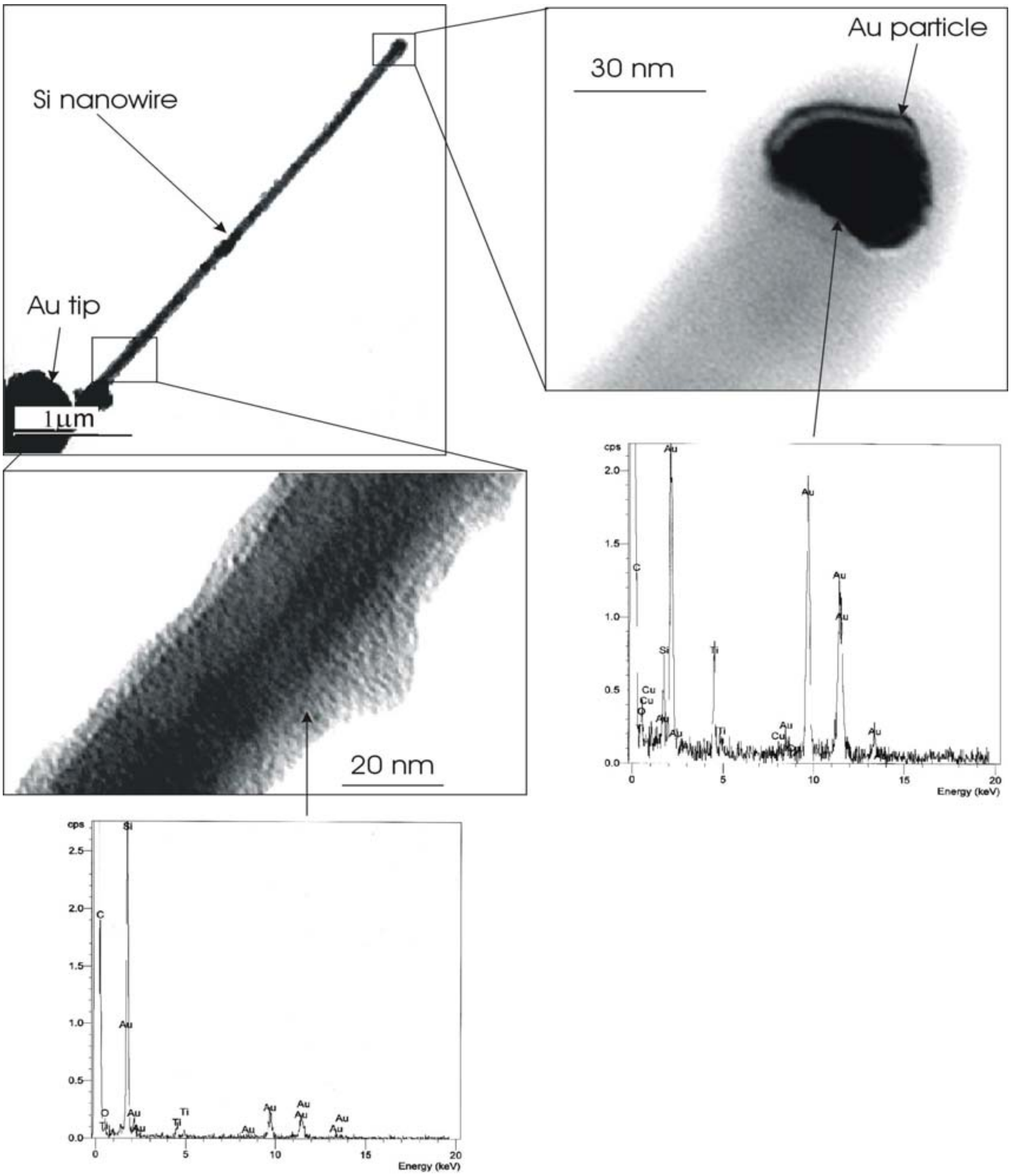

Figure 4.1.1. Si nanowire TEM image and elemental analysis.

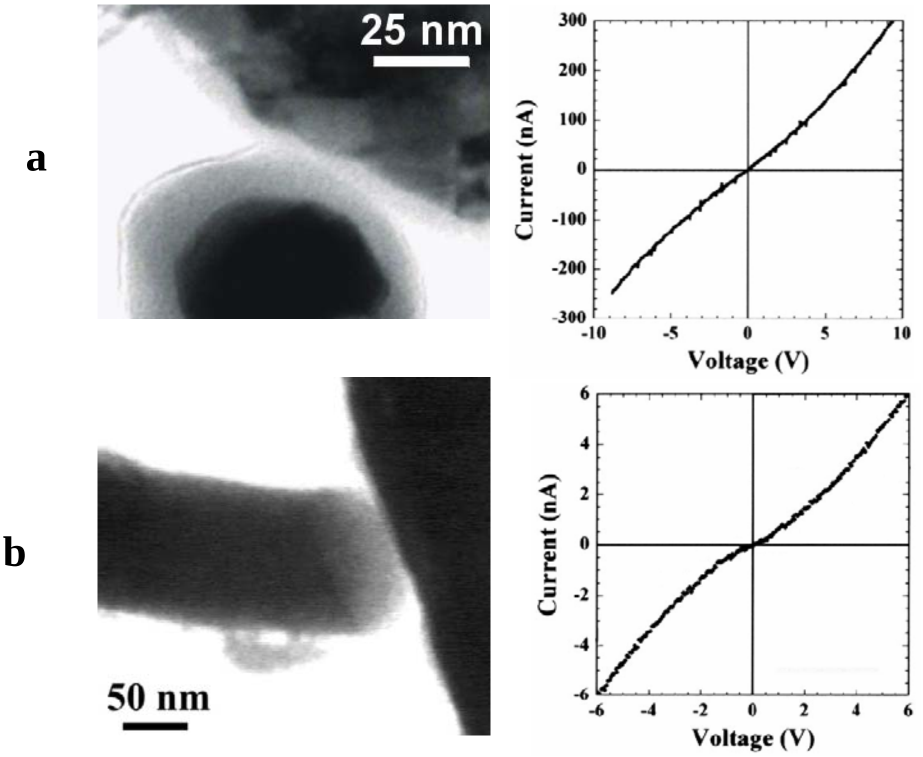

Figure 4.2.2. Nanowire contacts with Au electrode. (a) – Si nanowire contact and corresponding I(V) curve; (b) – Ge nanowire contact and I(V) curve.

It should be noted, that some obtained I(V) for Ge nanowires exhibit a nonconductive gap, which varied randomly (1–8 V) but typically was between 2 and 4 V. However, if nanowire was contacted by gold hemisphere on its end to the second electrode, it cause a significant decrease in the nonconductive gap and nearly linear *I*(*V*) behavior. These changes in the *I*(*V*) behavior with contact position suggest that there is an unstable native oxide layer on the Ge nanowires of varying thickness which acts as a barrier to the conductance. The resistance of the Ge nanowires varied significantly between 0.15 and 1 GΩ corresponding to resistivity of the order of $1\text{-}7\cdot10^{-1}$ Ω m. The higher resistivity suggests that the Ge nanowires are not as highly doped with gold as the Si nanowires having an impurity concentration of approximately 10^{14} cm^{-3}.

4.3 Elastic properties

Elastic properties of the nanowires were studied by mechanical bending of the nanowire with Au tip. Both Si and Ge nanowires were bended up to 70-90° without rupturing or any inelastic deformation (figure 4.3.1). After unloading the nanowire returned to the initial shape.

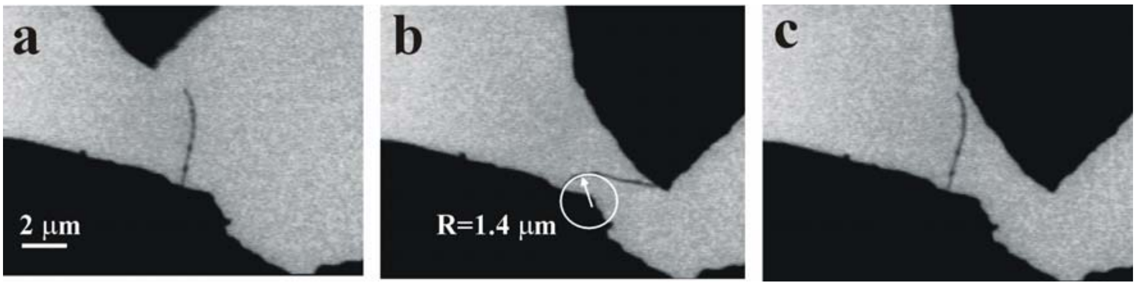

Figure 4.3.1. Mechanical deformation of Ge nanowire.

Internal strain can be easily estimated using following formula [68]:

$$\sigma = \frac{E \cdot r}{\rho} \tag{4.3.1}$$

where E – Young modulus (105 GPa for Ge), r – nanowire radius (90 nm), ρ – deformation radius (1400 nm). We found that nanowires do not ruptured at σ_{nw}=7 GPa, which is 50-140 times higher than wrecking strain for bulk Ge σ_{bulk}=50-150 MPa [69]. Such result was expected, because experimental rupture strain of bulk crystals is mainly determined by the micro cracks which lead to sample destruction and is lower than theoretically estimated.

4.4. Force interactions

The controlled approach of the electrode to the nanowire using piezodrive of TEM-STM holder was utilized to measure the distance at which the nanowire jumped to the gold contact (jump-to-contact distance). After contacting with the gold electrode, nanowire was withdrawn by the piezodrive, and jump-off-contact distance was measured. The jump-to-contact and jump-off-contact distances were measured at different applied voltages and can be directly related to the attractive forces between the nanowire tip and the gold electrode. The attractive van der Waals force (F_{vdW}) and electrostatic force (F_{elec}) between the nanowire and the gold electrode are countered by the opposing elastic energy (F_{elas}) exerted by the nanowire. The pull-on and pull-off forces between the nanowire and the Au electrode can be calculated using the spring constant of the nanowires, k.

Force interaction of a semiconducting nanowire with metal tip is very similar to AFM tip interaction with a solid surface and can be explained using AFM force curve (figure 4.4.1). The total attractive noncontact force (F_{TN}) acting on the nanowire is the sum of van der Waals force and electrostatic force, F_{TN}=F_{vdW}+F_{elec}. As the nanowire tip is moved toward the electrode (point a), the attractive forces acting on the nanowire tip steadily increase. At point *b*, the attractive force gradient exceeds the spring constant (dotted lines) of the nanowire ($dF_{TN}/dz > dF_{\mathrm{elas}}/dz = k$) and the jump-to-contact occurs [52] and comes to equilibrium at the intersection of $F(z)$ and the spring constant (point *c*). The jump-to-contact distance is the distance between points *b* and *c* and can be seen by TEM in our experiments.

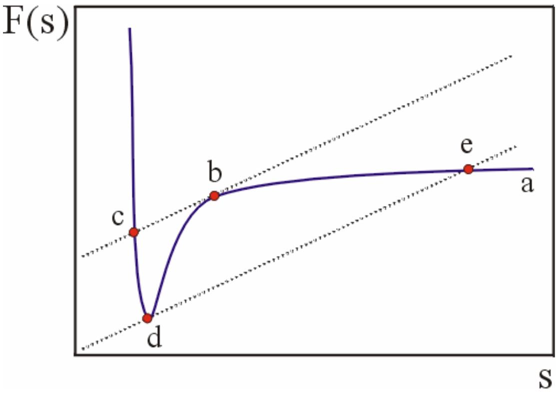

Figure 4.4.1. AFM force curve.

We can estimate the force constant of nanowire *k* using jump-to-contact distance (figure 4.4.2) if zero voltage applied between nanowire and metal electrode and assuming $F_{vdW} >> F_{elast}$ at small distances, using the following formula of van der Waals force for two interacting spheres [70]:

$$F_{VDW} = \frac{A}{6D^2} \cdot \frac{R_1 R_2}{(R_1 + R_2)} \tag{4.4.1}$$

$$\frac{dF_{VDW}}{dD} = \frac{A}{3D^3} \cdot \frac{R_1 R_2}{(R_1 + R_2)} = k \tag{4.4.2}$$

where A - Hamaker constant, D – jump-to-contact distance, R_1, R_2 – radius of spheres 1 and 2.

After nanowire contact the opposite tip, the adhesion force F_{adh} appears. Total contact force (F_{TC}) acting between metal tip and nanowire is a sum of attracting electrostatic force, van der Waals force, adhesion force and retracting elastic force: $F_{TC} = F_{\mathrm{vdW}} + F_{\mathrm{adh}} + F_{\mathrm{elec}} - F_{\mathrm{elas}}$. The jump-off-contact occurs (from point *d* to *e*) once the nanowire spring constant is greater than the total attractive force gradient ($dF_{TC}/dz < dF_{\mathrm{elas}}/dz = k$), which occurs at the minimum in the force curve (point *d*). If the voltage is set to zero (and consequently, the electrostatic force F_{elec}), the value of adhesion force F_{adh} can be extracted from force curve ($F_{\mathrm{vdW}} << F_{\mathrm{adh}}$).

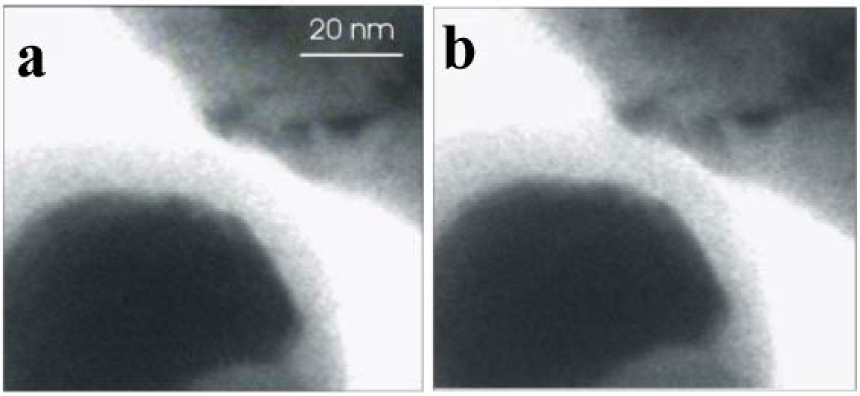

Figure 4.4.2. (a) – Si nanowire before jump-to-contact; (b) - after jump-to-contact.

4.5. Prototype of nanoelectromechanical device

We utilized same semiconductor nanowires for the development of NEMS, such as nanoelectromechanical programmable read-only memory (NEMPROM) devices, which require two stable conditions (ON/OFF).

The electrostatic force was used as driving force to bring nanowire into contact with electrode, where voltage is operating parameter. There are two possible regimes in the work of such device. In first regime (NEMPROM) retracting elastic force is smaller than attracting forces $F_{\mathrm{vdW}} + F_{\mathrm{adh}} > F_{\mathrm{elas}}$. Then nanowire remains in contact even if electrostatic force is set to zero. In second (nanorelay) regime elastic force is stronger than attracting forces $F_{\mathrm{vdW}} + F_{\mathrm{adh}} < F_{\mathrm{elas.}}$ If electrostatic force is set to zero, nanowire will be withdrawn due to strong elastic force. The strength of elastic force (F_{elast}) is determined by the nanowire – electrode distance and described by Hook law [71]:

$$F_{elast} = E \cdot D \qquad (4.5.1)$$

where E –Young modulus and D – nanowire-electrode distance. An example of a NEMPROM device made from a Ge nanowire is shown in the TEM frame sequence of figure 4.5.1. As the voltage is slowly increased, the device remains OFF figure 4.5.1(a). However, once the voltage is increased to critical voltage, jump-to-contact occurs as it seen in figure 4.5.1(b). The jump-to-contact is too fast to be viewed but the resonant frequency of this nanowire can be estimated to be in the MHz regime. The nanowire remains in contact (ON) with the electrode due to strong adhesion force even when the voltage is set to zero. These devices remain indefinitely stable demonstrating the nonvolatility of these devices for memory applications or other low leakage devices. Although these devices are highly stable, the NEMPROM devices can be switched OFF by mechanical motion. Figures 4.5.1(c) demonstrate that little shearing motion is required to overcome the attractive forces.

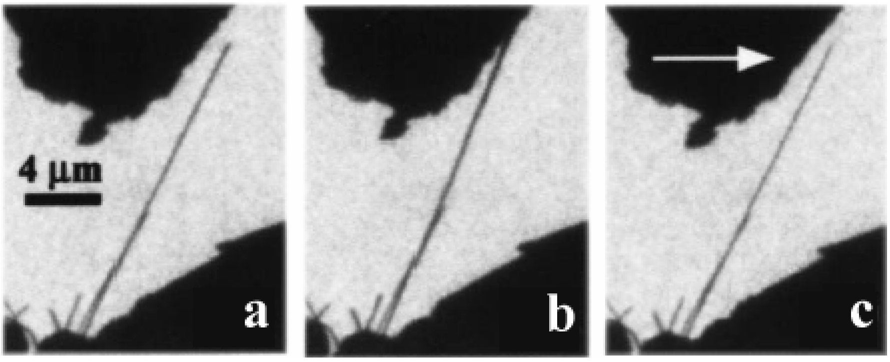

Figure 4.5.1. Demonstration of NEPROM principles. (a) – before voltage applied; (b) - applied voltage and nanowire jump-to-contact; (c) - voltage decreased to zero and nanowire jump-off- contact by small shear movement of metal tip.

The relatively large switching voltage (8.6V) utilized in this device was used for demonstration purposes so that the full deflection of the nanowire could be easily viewed. Smaller separation distances require much smaller switching potentials. However, there is a minimum distance (point *b* of figure 4.4.1) that must be maintained or the device will become unstable due to the strong van der Waals attractive forces resulting in jump-to-contact. NEMPROM devices can function at any distance between points *b* and *e* of the force– distance curve in figure 4.4.1. The NEMPROM devices synthesized in our experiments were robust; each nanowire tested could be switched ON and OFF multiple times (20–50) without noticeable deformation or fracture. However, further experimentation is required to determine their viability in future devices.

4.6. Comparison of AAO template synthesized and free nanowires

Template synthesized nanowires have much higher resistance of 80-1000 Ωm and 140-3000 Ωm for nanowires with mean diameters of 100 nm and 50 nm respectively in comparison to free nanoparticle catalyst synthesized nanowires (0.1 Ω m). Lower than the bulk (0.66 Ω m) resistance of catalyst grown nanowires can be explained by doping with impurity atoms which greatly increase charge carrier concentration. VLS synthesis of Ge nanowires demands high temperatures (at least 400° C). Material of nanowire precursor is usually introduced into reactor in gaseous form and decomposes at catalyst nanoparticles. Metal nanoparticles absorb released Ge atoms and form eutectics. Following feed of precursor material cause eutectics oversaturation and crystallization of Ge, thus nanowire nucleates and grows. Harvested nanowires may be doped with Au catalyst atoms (in our case doping concentration was 10^{14} cm^{-3}). In contrast with catalyst grown nanowires, template grown nanowires can be synthesized no doped, as it was shown in chapter 3.

Many other properties of both template and nanoparticle catalyst-seeded nanowires are determined by production method and compared below. Diameter of nanowires strongly depends on precursor nanoparticles diameter (figure 4.6.1). Nanowire diameter can be adjusted by choosing precursor nanoparticles of proper size. However, it should be noted that at high temperatures metal catalyst nanoparticle becomes liquid and can spontaneously form two metal droplets and resulting into two nanowires. This situation is illustrated at figure 4.6.1, where the green arrow points to the splitted nanoparticle. Nanowire length and growth direction also cannot be controlled with high precision even at epitaxial growth.

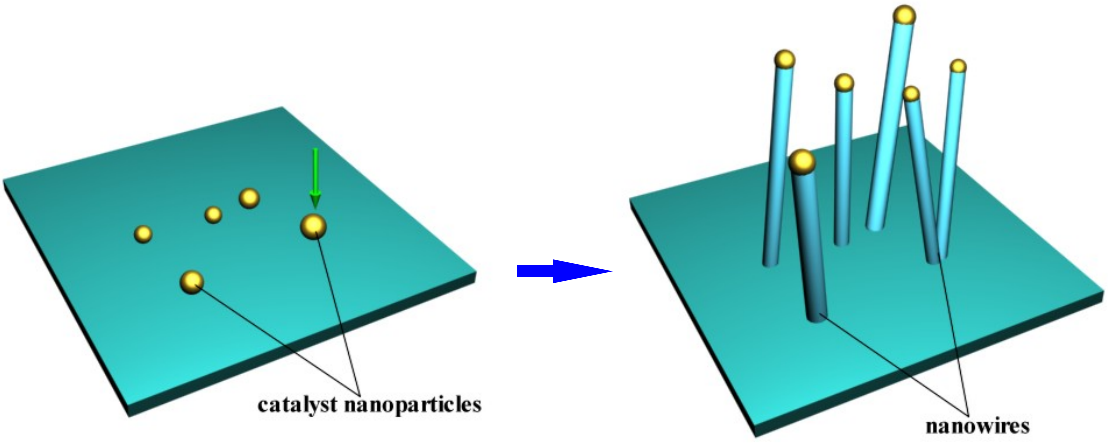

Figure 4.6.1. Scheme of nanowire synthesis based on metal catalyst nanoparticles.

Template assisted synthesis method has many advantages in comparison with nanoparticle catalyst growth technique. Nanowires grown inside AAO matrix are highly ordered and perpendicular to the membrane surface plane (figure 4.6.2). Nanowires diameter depend on empty AAO pore size, which may be easily adjusted from 10 to 200 nm, thus diameter can be controlled. High nanowire packing density may be achieved using template synthesis (in our case $1.4 \cdot 10^{10}$ and $9 \cdot 10^{8}$ cm^{-2} for 50 and 100 nm nanowires respectively). Nanowires length is equal to membrane thickness (from 100 nm to 250 μm).

Free nanowires after introduction to ambient atmosphere oxidize and adsorb molecules from air, which significantly influence its electroconductive properties [72]; in contrast, the matrix serve as a natural shield and nanowires are not oxidized at ambient conditions. Aluminum oxide is known as good heat conductor and heat can be effectively evacuated from nanowires, which is essential for nanoelectronics applications. Membrane with nanowires inside can be mechanically polished and etched by wet or ion etching. Membrane can be also completely dissoluted and nanowires released.

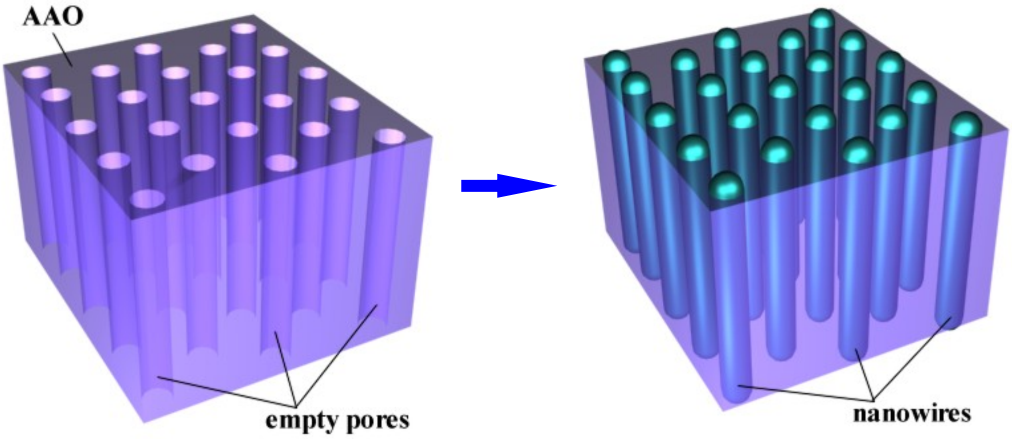

Figure 4.6.2. Scheme of AAO template assisted nanowire synthesis.

AAO assisted nanowire synthesis may be successfully combined with conventional semiconductor technologies. Aluminium film can be formed on the semiconductor wafer surface, anodized and converted into AAO [73]. Different methods could be applied to fill AAO pores with metal or semiconductor materials and thus creating nanowires [13, 74]. However, connection of nanowires to each other or to other components is required to integrate nanoobjects into functional device. DNA molecule and its architectures are possible candidates for the role of connecting nanocomponents and they are investigated in the next chapter.

CHAPTER 5

3D DNA ARRAYS ON Au(111)

5.1. Structure

Spatially distributed DNA oligomer arrays were created on the gold surface (111) by incorporation of thioalkyalted-DNA into mercaptohexanol (MCH) monolayer (figure 5.1.1) and their properties were investigated.

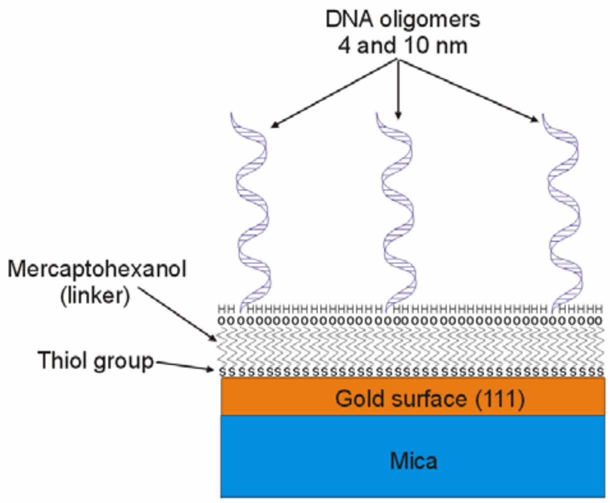

Figure 5.1.1. Schematics of DNA array on Au (111) surface.

Density of DNA molecules on a surface was fitted to achieve situation when AFM tip statistically contacts only one DNA oligomer for probing its electroconductive properties. Structure of diluted DNA array was investigated using AFM in Tapping Mode. Figure 5.1.2 shows topography and phase response images of DNA array on the surface. DNA oligomers appear as protrusions in height and phase images. Positive phase response means that DNA molecules are stiffer in comparison with surrounding MCH layer. Our measurements show that DNA oligomers are well distributed on the surface. DNA density at the surfaces was estimated from AFM measurements. It increased nonlinearly with the DNA mole fraction in the solution. Double-stranded DNA density was $(2\text{-}3)\cdot 10^{10}$; $1\cdot 10^{11}$, and $(2\text{-}3)\cdot 10^{11}$ chains/cm^2 for monolayers formed from solutions containing DNA mole fractions of 0.1%, 1%, and 50%, respectively. In the case of 50% concentration, the DNA density at the surface in reality might be higher because it was problematic to resolve individual DNA molecules in close packed groups. The density of single-stranded DNA oligomers on the surface was apparently lower than that for double-stranded at the same concentration.

The maximum DNA oligomer density in our spatially distributed DNA monolayers was lower by more than an order of magnitude than in densely packed monolayers of DNA oligomers. The coverage of HS-ssDNA in mixed DNA oligomers-alkanethiol monolayers was reported to be (1-10)·10^{12} chains/cm^2 [75, 76]. However, it is difficult to compare the data because we used different surface coating methods.

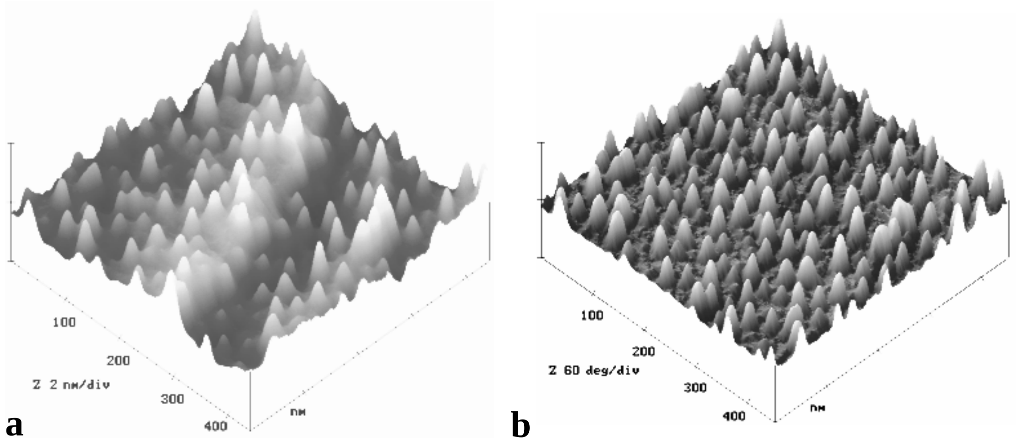

Figure 5.1.2. (a) - tapping AFM images of DNA-array surface topography; (b) - phase image.

Scanning in lift mode was applied to investigate whether DNA oligonucleotides extend vertically upward from the monolayer in such low density coatings. Structures with the same distribution were observed when measuring the phase response in the lift-mode: then, repeated scans at increased distances from the surface revealed the structures with an identical spatial arrangement. Phase response in the lift mode was negative in most cases. The maximum lift height at which the phase response was still observed depends on setpoint ration r_{sp}, oscillation amplitude A_0, and the length of DNA (table 5.1.1). The difference in the lift height for 10 and 4 nm long double-stranded DNA oligomers was almost equal to that in the length of DNA oligomers and served as evidence that DNA oligomers are not lying on the surface but were extended vertically upwards from the monolayer.

Table 5.1.1. The maximal tip lift height (in nm) at which DNA structures were still observed at different setpoint ratio r_{sp}. Tapping amplitude A_0=45 nm.

r_{sp} \ DNA type	10 nm double-stranded	4 nm double-stranded	4 nm single-stranded
0.67	11	7	6
0.36	21	14	13

The lift height at which the structures were observed was almost the same for 4 nm long single- and double-stranded DNA oligomers (table 5.1.1) which implies that single-stranded DNA oligomers were also extended vertically from the surface in mixed monolayers. Thus diluted DNA oligomer array is appropriate system to measure DNA conductivity by sharp electroconductive probe because molecules are perpendicular to surface and tip statistically will contact only one or few DNA molecule. Both STM (Scanning Tunnelling Microscope) and conductive AFM were used for conductivity measurements. STM probe is rigid gold tip with infinitely large force constant, thus no jump to contact occurs and tip may be gradually approached to the sample surface. In contrast, AFM with low spring constant cantilevers allow to measure small interaction force between the metal tip and metal surface coated with DNA.

5.2. Force interactions

Prior interpretation of any conductivity measurement results maden by conductive AFM tip it is necessary to analyze all acting forces, which potentially can disturb DNA oligomer configuration in contact with conductive tip.

Non-contact forces. The electrostatic force depends on the distance, bias, tip geometry and dielectric constant of the gap between two electrodes (AFM tip and sample surface). Dielectric constant of the media between the tip and a sample was composed of dielectric constants of MCH, DNA, adsorbed water and air. Typical electrostatic force dependence on voltage for 10 nm long DNA oligomers coated surface is presented in figure 5.2.1. The force value practically did not depend on bias polarity. It means that there was not charge trapped on the tip or in the MCH and DNA monolayers. All charges inside monolayers were compensated.

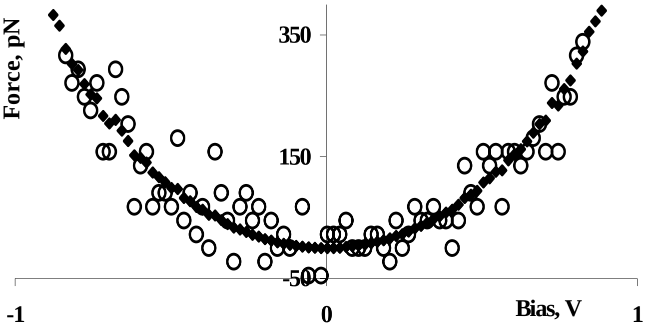

Figure 5.2.1. Electrostatic force curve on DNA array surface.
Empty circles – experimental data, filled diamonds – fitted data.

Experimental data were fitted using theoretical electrostatic force formula for sphere plane interaction at distances shorter than the tip diameter [77]:

$$F_{elec} = \pi\varepsilon\varepsilon_0 RV^2 / D, \tag{5.2.1}$$

where ε is the average dielectric constant of the gap, R - the tip radius, V - voltage, D - distance between tip and Au(111) surfaces. Values of ε used in the data fitting were taken equal to 1, 81 and 2 for air, water and MCH respectively, according to ref. [78]. The tip-surface distance value was calculated as a sum of jump-to-contact distance and monolayer thickness and was 17 for DNA and 10 nm for MCH surface coatings. Theoretical curve fitted the experimental data when the thickness of water layer on the Au tip, Au substrate surface, and MCH was around 2 nm. This is in good agreement with data about the thickness of water layer on gold surfaces [79].

Van der Waals interaction force F_{vdW} between a sphere and plane surface [52] is equal to:

$$F_{vdW} = AR / 6D^2 , \tag{5.2.2}$$

where A – Hamaker constant, R – tip curvature radius, D – tip-surface distance. Tip radius was measured by TEM and was R=30 nm. For D=4 nm (typical distance before jump-to-contact) and Hamaker constants $4 \cdot 10^{-19}$, $1.5 \cdot 10^{-19}$ and $0.5 \cdot 10^{-19}$ J accordingly for metals, water and hydrocarbons, the corresponding F_{vdW} forces are 125, 47 and 16 pN respectively [70].

Jump-to-Contact. Jump-to-contact distance was about 4-5 nm for both cantilevers with force constant 0.1 and 0.16 N/m, and corresponding force acting on the tip was 500-600 pN. The value of the electrostatic force at bias 1 V just before jump-to-contact was app. 500 pN which exceeds van der Waals force, and is mostly responsible for jump-to-contact. After contact the contribution of electrostatic force and van der Waals force in the total force is negligibly small in comparison to much higher adhesion force.

Contact forces. When the tip is in the contact with the liquid layer, the adhesion force appears due to Laplace pressure acting over the area where the meniscus contacts the tip [77, 79]. The adhesion force F_{adh} between tip and surface can be described by the following formula:

$$F_{adh} = 4\pi R \gamma \cos \theta , \tag{5.2.3}$$

where R – tip radius, γ is the surface tension of water and θ the contact angle. For water γ=73 mJ/m^2 [79], R=30 nm and at $\cos\theta$=1, and using these parameters we found F_{adh}=27.5 nN. For hydrocarbons γ=20-25 mJ/m^2 [79] and at the same R and θ the resulting force is equal to F_{adh}=8.5 nN. The experimental values of adhesion forces found from tip jump-off distance on force curve varied between 10 - 27 nN for both

DNA and MCH monolayer at withdraw speeds 90 μm/s. Large dispersion of the results we observed may be explained by nonuniform thickness of crystalline water film on the surface.

Even at presence of high adhesion force the tip does not completely penetrate the water layer on gold surface and on top MCH. This conclusion is based on the absence of tunnelling current immediately after the jump-to-contact. A few effects may be responsible for repulsive tip-surface interaction after the jump-to-contact. The jump-to-contact and following tip movement may be too fast to cause water flow out from the confinement area between the tip and surface. Repulsive hydrostatic force F_{hyd} will act on the tip in this case. The hydrostatic force at certain speed v can be calculated using Raynolds formula for a planar surface and tip with radius R [80]:

$$F_{hyd} = 6\pi R^2 \eta v / D , \tag{5.2.4}$$

where η is viscosity (for water 0.01002 g/(cm s) [81]), D - distance between the tip and sample. The calculated force values are $1 \cdot 10^{-5}$ nN and $2 \cdot 10^{-7}$ nN for approach speeds 2900 nm/s and 60 nm/s, respectively, at tip-sample distance of 1 nm. Thus, the impact of hydrostatic force in the repulsive interaction can be neglected.

Another source of the repulsive interaction with the tip may be the viscoelastic response of MCH and DNA monolayers. Possibly, the viscoelastic elements have not enough time to relax at fast approach. The time interval when the tip is in the contact with monolayers is 5-10 ms and 50-100 ms for approach speeds 2900 nm/s and 60 nm/s, respectively, which is comparable with viscoelastic response time for these monolayers. Viscoelastic response was observed as difference in surface stiffness at different approach speeds. The repulsive interaction decreases with approach speed decrease and almost vanishes at the speed 60 nm/s (figure 5.2.3).

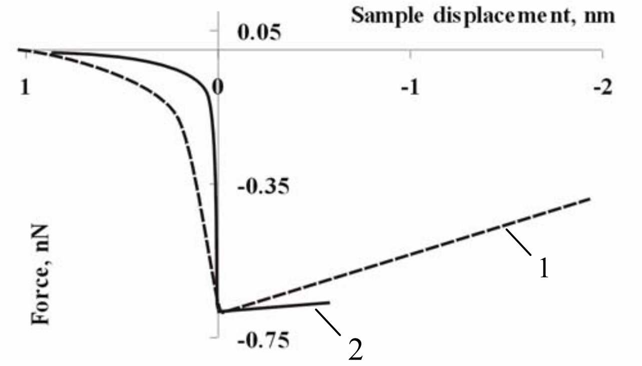

Figure 5.2.3. Dependance of repulsing force on approach speed. Curve 1 - 2900 nm/s, curve 2 - 60 nm/s.

The relative surface stiffness was calculated as a ratio of cantilever displacement to the sample displacement. The sample displacement increases on softer surfaces and thus the relative surface stiffness decreases. The surface stiffness decrease at lower approach speed for both DNA and MCH monolayers (table 5.2.1), which is an evidence of viscoelastic behaviour of both MCH and DNA monolayers.

Table 5.2.1. Relative stiffness of 10 nm long DNA, MCH on Au(111) and Au surfaces, bias 1 V.

Speed, nm/s	DNA 50%	DNA 1%	MCH	Au surface
2900	0.75	0.7	0.7	1.0
1200	0.63	0.56	0.67	
60	0.55	0.44	0.62	1.0

The water layer on a bare gold surface was stiffer than cantilever for all approach speeds (so called crystalline water). It means that there is no viscoelastic effect on the gold surface coated with water layer. Water molecules are usually present on gold surface at ambient conditions. We conclude that they are arranged in form of a rigid film similar to [82]. The effective stiffness decreases with lowering of approach speed for DNA monolayers. Stiffness value was higher in DNA case in comparison with MCH monolayer at high approach speed. This may mean that viscoelastic response time for such structures is shorter than for close packed MCH monolayer. The changes in the stiffness depend on DNA density on the surface. The effective stiffness of more diluted DNA array is lower in comparison with high density array obviously due to smaller amount of DNA molecules involved in the contact.

5.3. Electroconductive properties

Different measurement algorithms were tried to probe electrical transport through DNA oligomer in this work. First straightforward approach was measuring of I(V) curves by STM (Scanning Tunnelling Microscope) at different tip-sample distances (figure 5.3.1). I(V) characteristics were similar for MCH and DNA coatings from the mechanical contact till predetermined resistance of 0.6 GΩ (0.015nA, 1V). Small current setpoint was chosen to avoid deep penetration of tip into monolayer as well as possible monolayer damage and tip contamination.

These curves can be fitted for both DNA and MCH case using the following formula [83]:

$$I = A\left[6.2\times10^{10}/\Delta s^{2}\right]\left\{\bar{\varphi}\exp(-1.025\Delta s\bar{\varphi}^{\frac{1}{2}})-(\bar{\varphi}+V)\exp\left[-1.025\Delta s(\bar{\varphi}+V)^{\frac{1}{2}}\right]\right\},\ \text{where}\ \bar{\varphi}=\frac{1}{\Delta s}\int_{s_1}^{s_2}\varphi(x)dx$$

(5.3.1)

where A is the tunneling region area, Δs - the distance between electrodes, V – voltage bias, φ = 0.9eV of MCH molecule with water coating [84] and assuming that DNA molecule is a metal wire.

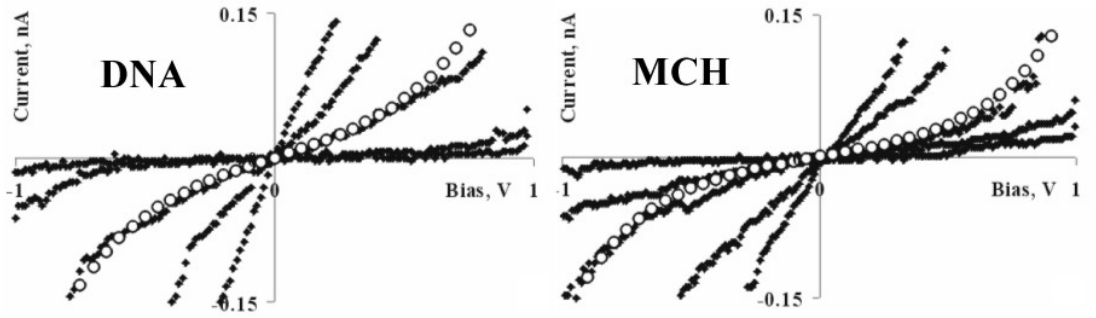

Figure 5.3.1. I(V) curves obtained by STM at different tip-sample distances (step height app.1Å, higher current correspond to closer tip to surface position). Filled diamonds correspond to experimental data, empty circles to fitting data.

Comparing I(V) curves of Figure 5.3.1 we can suppose that DNA behaves as a metal wire assuming proper contact configuration (figure 5.3.2(a)). Curves are very similar, which can be interpreted as negligible resistance of DNA molecule. However it is possible that DNA molecules diffused from the contact under high load (figure 5.3.2(b)). Acquisition time for one I(V) characteristic was 50-100 ms and tip-sample contact time exceed DNA-MCH viscoelastic response time considerably [85]. That is why alternative method of DNA oligomer conductivity probing was applied.

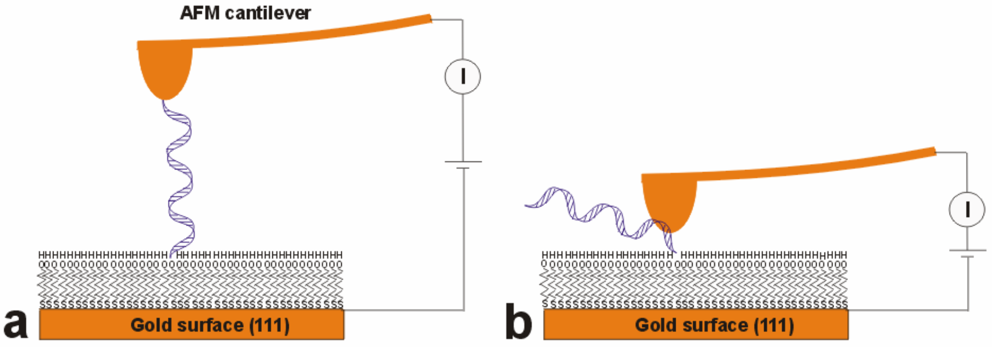

Figure 5.3.2. Schematics of DNA conductivity probing by C-AFM with gold coated cantilevers. (a) – in case of metallic conductivity of DNA; (b) – DNA is nonconductive.

Current vs. displacement I(s) measurements with simultaneously detected force vs. displacement F(s) were expected to be more adequate than I(V) measurements because tip-monolayer interaction time was much shorter. Typical I(s) and F(s) curves obtained by conductive AFM are presented on figure 5.3.3(a). Tunnelling current has appeared only after 4 nm sample displacement. Sample displacement here mean cantilever holder displacement relative to sample. Tip displacement inside monolayer is smaller than sample displacement because of cantilever elastic deformation. Resistance of 6 GΩ (0.15nA, 1V) was established after 8.5 nm sample displacement, which correspond to 1.5 nm tip displacement inside the 10 nm long DNA monolayer. At predetermined resistance 6 GΩ and applied bias 1 V the tip displacement was 1-2 nm for MCH and DNA coating.

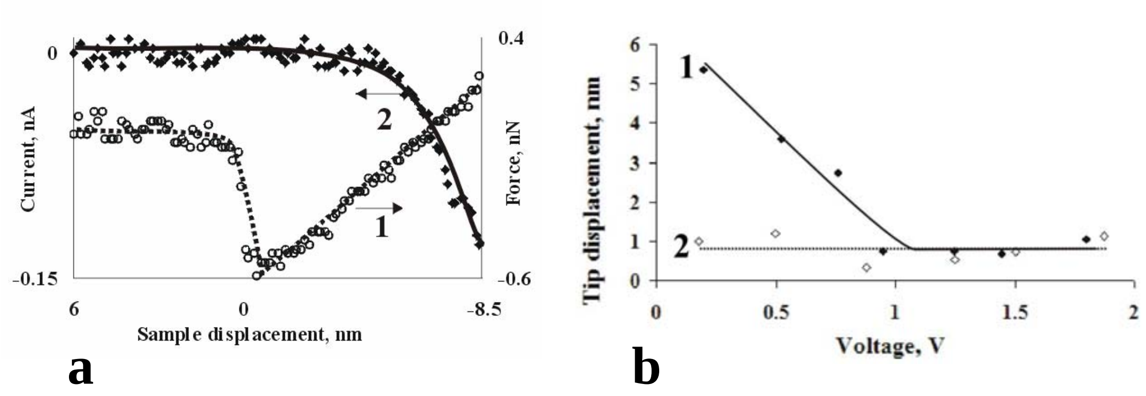

Figure 5.3.3. (a) - typical F,I(s), curve 1 – force, 2 – current. (b) – sample displacement depending on applied voltage, curve 1 – DNA, curve 2 – bare gold.

The tip displacement on DNA array coated surface increases to the distance comparable with DNA length, when voltage was decreased till 0.02V (0.1GΩ) as shown at figure 5.3.3b. On bare gold the displacement of the tip remain the same at voltage 0.02V (0.1 GΩ) within experiment accuracy. It means that current flows through DNA oligomers at voltages higher than 1V, however it cannot flow at lower voltages. We explain such behaviour by nonconductive nature of DNA oligomers. DNA conductivity at high voltage may be provided by dissociated water molecules similar as in [86].

Summarizing this chapter we can conclude that spatially distributed DNA oligomer array is perspective template for nanoobject assembly at solid surface due to oligomers vertical arrangement and ability to hybridize with complementary single strand DNA molecules. However, DNA oligomers do not behave as metallic molecular wire and can not be used for electrical addressing of nanoobjects without metallization treatment.

Chapter 6

Possible applications

6.1. Possible devices

Semiconducting nanowire arrays inside AAO potentially may be utilized in nanoelectronics and nanofotonics. In this chapter two possible application of nanowire array are proposed, where its high density packing can be exploited. Semiconducting nanowire arrays potentially may be used for creation of photosensitive matrix (figure 6.2.1). Nanowires can serve as photoresistors (as it was demonstrated in chapter 3) or as nanowire based diodes [87]. Optical image is projected onto nanowire array through transparent electroconductive electrode. Adsorbed light generate excess charge carriers which increase conductivity of illuminated nanowires. The current through nanowires is measured, and the photogenerated increase of current can be detected in illuminated nanowires. Thus optical image can be reconstructed from acquired current map.

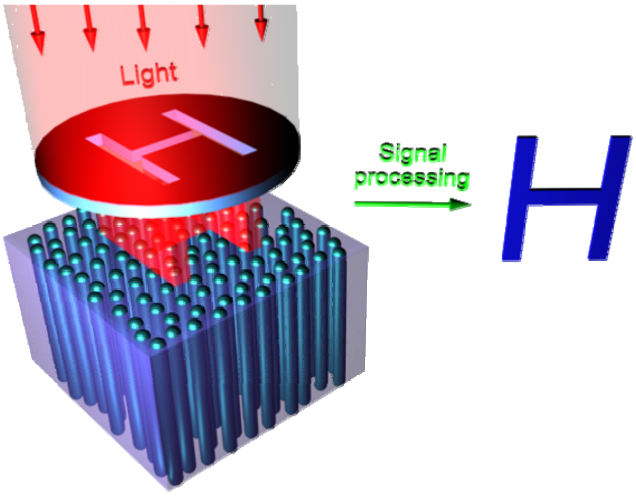

Figure 6.1.1. Photosensitive matrix based on nanowire array in AAO membrane.

Planar design of “on-chip” realization of NEPROM device [17] is suitable for mass production, however it is difficult to achieve high packing density of nanodevices using 2D approach (figure 1.1a). NEPROM may be designed also in 3D array configuration, where nanowires are perpendicular to the surface plane. This approach may yield device packing density up to 10^9-10^{11} cm^{-2}. Here we propose creation of 3D NEPROM array inside porous AAO membranes as shown in figure 6.1.1. Nanowires should be mounted on the bottom electrode and surrounded by empty space. AAO pore walls will limit movements of nanowire and support upper electrodes. Using simple calculations one can estimate that Ge nanowires of 100 nm in diameter will form stable device at maximal AAO membrane thickness of 20 μm.

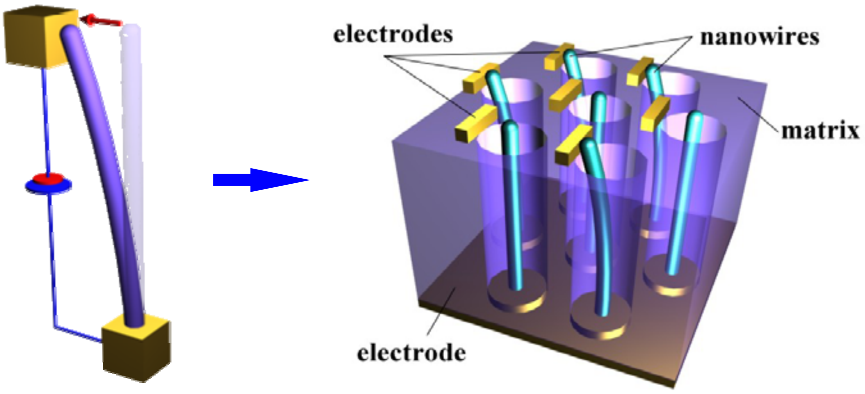

Figure 6.1.2. Integration of single NEMPROM into high density NEPROM array based on 3D nanowire architecture inside AAO matrix.

6.2. Contacting challenges

Each nanowire in the array should be electrically contacted to utilize full advantage of high density packing. That is extremely challenging task due to ultra small dimensions of nanowires. However we can assume three possible solutions adjusted to the geometry of nanowire arrays inside AAO membranes.

Classical approach to contact 100 nm nanowires is high resolution photolithography. Nanowires could be contacted using crossed electrode strips geometry as it shown at figure 6.2.1. Addressing top and complimentary bottom stripe electrodes each nanowire in array could be probed.

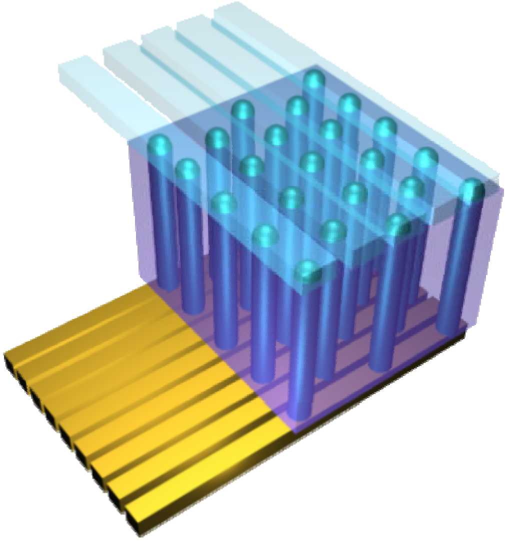

Figure 6.2.1. Contacting nanowires in array by addressing of crossed electrode stripes formed by photolithography.

In case of nanowires with smaller diameter more sophisticated techniques could be applied, such as contacting by sharp C-AFM tip, as was demonstrated in chapter 3. Potentially this method may be used for realization of both photosensitive matrix and NEPROM array. In case of photosensitive matrix the membrane with nanowires is coated with transparent electrode from one side. We can use conductive AFM tip as second electrode from the opposite membrane side. Optical image can be reconstructed from current map, provided by C-AFM. Realization of NEPROM array may be similar. C-AFM can “write” bits of information by applying high voltage to force nanowire to jump to contact (“On” position) and “read” information stored in array by scanning with low voltage applied and recording the current map. Nanowire in “On” position will be conductive and nonconductive in “Off” position. Information can be erased in array by heating the whole device, shaking or filling it with liquid. This approach is expensive due to complicated instrumentation involved. Nevertheless, AFM technique evolves quickly and in future the control electronics may be integrated in simple chip and become cheap enough [88].

Alternative approach of contacting individual nanocomponents may be application of DNA molecule which can connect nanowires and macroelectrodes. 3D DNA array architecture may be used in this case. Our DNA arrays have packing density 10^{10}-10^{11} cm^{-2} which is higher than nanowire packing density and thus fit very well to be adsorbed on top of nanowires. DNA molecule has smaller diameter in comparison with semiconducting nanowires (app. 2 nm depending on conformation) and potentially unlimited length [42]. Moreover, DNA molecule is sufficiently soft and can be bent easily, which is favorable for wiring applications. We found that DNA molecule is a poor electro current conductor (chapter 5). However, DNA may be metallised and become excellent electroconductive metallic wire [89]. It is necessary to solve many serious problems to bring these projects into reality, such as insulation of metalized DNA and elimination of contact resistance. This approach is extremely promising as simple, flexible and inexpensive. The work on integration of organic molecules with nanowire in array recently has been started in the Institute of Chemical Physics.

Chapter 7

Conclusions and Thesis

CONCLUSIONS AND NOVELTY OF RESULTS

In this work both organic and inorganic nanowire architectures created via self-assembly methods were investigated: ordered 3D Ge nanowire arrays and spatially distributed 3D DNA arrays.

To the best of our knowledge this is the first complex study on electrical characterization of germanium nanowire arrays inside AAO. Structure, electroconductive and photoconductive properties were investigated. Nanowires inside membranes are found to be well ordered. The packing density of nanowires inside AAO matrix for 50 and 100 nm nanowires is established to be $1.4 \cdot 10^{10}$ and $9 \cdot 10^{8}$ cm^{-2} respectively. Contact problem of nanowire / electrode is investigated and contact optimization procedure is found. Electro conductivity of individual germanium nanowires within AAO is studied and compared with averaged conductivity over large amount of nanowires in array. Nearly all nanowires inside membrane are found to be electroconductive and exhibit intrinsic conductivity. New information on photoconductivity and photodynamics of germanium nanowire array inside AAO is acquired. We think that nanowire arrays possess substational potential for utilization in opto- and nanoelectronics. The development of cheap and simple techniques for nanowires integration with conventional semiconductor technology is a serious challenge, and, to our opinion, the solution of this problem may be of great advantage for microelectronic industry.

Electroconductivity of nanoparticle (Au) catalyst synthesized free Si and Ge nanowires is studied and nanowire / electrode contact area is simultaneously visualized. Electroconductivity of free nanowires is compared with electroconductivity of AAO template synthesized nanowires and it is found that in the first case it is much higher (10^{3}-10^{4} times) due to doping with Au atoms of catalyst nanoparticles. Nanoelectromechanical interactions of single semiconducting nanowires with metal electrodes are investigated for the first time. High elasticity (higher than elasticity of bulk material) of single nanowires is also demonstrated. Information on mechanical properties and acting forces was collected and used to propose and demonstrate some principles of nanoelectromechanical device (NEPROM memory element) based on single semiconducting nanowire. This result is important for nanowire application for the construction of nanoelectromechanical systems (NEMS). Advances in NEMS technology may develop into specific and superior substitutes for conventional electronic devices.

Novel 3D DNA architecture of oligomer array on Au (111) surface is researched. DNA oligomer surface density can be varied in range 10^{10}-10^{11} cm^{-2} depending on DNA concentration. Structure of oligomer array is studied and vertical orientation of DNA molecules is proved. Viscoelastic behavior of DNA oligomers attached to solid surface is demonstrated. Electroconductivity of individual DNA oligomers was probed directly by conductive AFM tip and DNA oligomers found to be poor current conductors. Similar DNA oligomer arrays architectures can be utilized in many applications in both bio- and nanotechnology.

THESIS

1. Electrical properties investigation method for individual nanowires inside AAO matrix using conductive AFM is elaborated and its applicability demonstrated.

2. Method of nanowire/electrode contact improvement for nanowires inside AAO matrix using selective chemical etching is found.

3. Ge nanowires synthesized with SCF inclusion method in AAO template are proved to be electroconductive and are demonstrated to exhibit photoconductivity.

4. Principles of nanowire based nanoelectromechanical device (NEPROM) operating are proposed and prototype of such device is demonstrated.

5. Method for electrical probing of DNA oligomers in 3D array on solid surface by conductive AFM is elaborated and its applicability demonstrated.

CHAPTER 8

REFERENCES

[1] Document of European Nanoelectronics Initiative Advisory Council: Strategic Research Agenda, ENIAC, 2005 (http://cordis.europa.eu.int/ist/eniac/home.html).

[2] T.Ando, Y.Arakawa, K.Furuya, S.Komiyama, H.Nakashima. Mesoscopic Physics and Electronics. *Springer-Verlag*, Berlin, 1998.

[3] L.Guo. *Proceedings of conference TNT-2004*, 31, 13-17 September, 2004.

[4] R.Cowburn. *Proceedings of conference TNT-2005*, 23, 29 August – 2 September, 2005.

[5] S.-W.Chung, D.Ginger, M.Morales, Z.Zhang, V.Chandrasekhar, M.Ratner, C. Mirkin. *Small,* 64, 1, 2005.

[6] L.Salmeron. *Materials Today*, 22, October 2003.

[7] L.Pavesi, L.Dal Negro, C.Mazzoleni, G.Franzoa, F.Priolo. *Nature*, 408, 440, 2000.

[8] Q.Wan, T.Wang, C.Lin. *Nanotechnology*, 14, L15, 2003.

[9] M.Huang, S.Mao, H.Feick, H.Yan, Y.Wu, H.Kind, E.Weber, R.Russo, P.Yang. *Science*, 292, 1897, 2001.

[10] C.Thelander, T. Martensson, M.Björk, B. Ohlsson , M. Larsson, L Wallenberg, L.Samuelson. *Appllied Physics Letters*, 83**,** 2052, 2003.

[11] M.Bjork, B.Ohlsson, C.Thelander, A.Persson, K.Deppert, L.Wallenberg, L.Samuelson. *Appllied Physics Letters*, 81, 4458, 2002.

[12] J.Hu, T.Odom, Ch.Lieber. *Accounts of Chemical Research*, 32, 435, 1999.

[13] A.Bard. Integrated Chemical Systems. *John Wiley and Sons, Inc.,* New York, 1994.

[14] M.Yazawa. *Apllied Physics Letters,* 58, 1080, 1991.

[15] K.Haraguchi, T.Katsuyama, K.Hiruma, K.Ogawa. *Appllied Physics Lett*ers, 60, 745, 1992.

[16] Y.Huang, X.Dua, C.Lieber. *Small*, 1, 142, 2005.

[17] S.Lee, D.Lee, R.Morjan, S.Jhang, M.Sveningsson, O.Nerushev, Y.Park, E.Campbell. *Nano Letters,* 4,10, 2027, 2004.

[18] T.Crowley, K.Ziegler, D.Lyons, D.Erts, H.Olin, M.Morris, J.Holmes. *Chemistry of Materials*, *15,* 3518, 2003.

[19] C. Schonenberger, B. Zande, L.Fokkink, M. Henny, C. Schmid, M. Kruger, A. Bachtold, R. Huber, U. Staufer. *Journal of Physical Chemistry B*, 101, 5497, 1997.

[20] P.Nguyen, D.Pearson, R.Tonucci, K. Babcock, *Journal of Electrochemical Society*, 145, 247, 1998.

[21] G.Thompson, G. Wood. *Science and Technology*, *23*, 205, 1983.

[22] J. Diggle, T. Downie, C. Goulding. *Chemical Reviews,* , *69*, 365, 1969.

[23] Y. Li, D. Xu, Q. Zhang, D. Chen, F. Huang, Y. Xu, G. Guo, Z. Gu, *Chemistry of Mater*ials, 11, 3433, 1999.

[24] G. Schmid, M. Baumle, M. Geerkens, I. Heim, C. Osemann,T. Sawitowski, *Chemical Society Reviews*, 28, 179, 1999.

[25] Yu, Y. J.; Chung, S. W.; Heath, J. R. *J. Phys. Chem. B* 2000, *104*, 11864.

[26] Shan, Y.; Kann Kalkan, A.; Peng, C.-Y.; Fonash, S. J. *Nano Lett.* 2004, *4*, 2085.

[27] Wang, D.; Wang, Q.; Javey, A.; Tu, R.; Dai, H.; Kim, H.; McIntyre, P. C.; Krishnamohan, T.; Saraswat, K. C. *Appl. Phys. Lett.* 2003, *83*, 2432.

[28] Hanrath, T.; Korgel, B. A. *J. Phys. Chem. B* 2005, *109*, 5518.

[29] Liu, C. H.; Yiu, W. C.; Au, F. C. K.; Ding, J. X.; Lee, C. S.; Lee, S. T. *Appl. Phys. Lett.* 2003, *83*, 3168.

[30]A.Yakimov, A.Dvurechenskii, A.Nikiforov, Y.Proskuryakov. *Journal of Appllied Physics*, *89*, 5676, 2001.

[31] J.Wang, M.Gudiksen, X.Duan, Y.Cui, C.Lieber. *Science*, 293, 1455, 2001.

[32] H.Kind, H.Yan, B.Messer, M.Law, P.Yang. *Advanced Materials*, 14, 158, 2002.

[33] S.Mathur, S.Barth, H.Shen, J.-C.Pyun, U.Werner. *Small*, 1, 713, 2005.

[34] D.Pena, J.Mbindyo, A.Carado, T.Mallouk, C.Keating, B.Razavi, T.Mayer. *Journal of Physical Chemistry B*, 106, 7458, 2002.

[35] S.Han, W.Jin, D.Zhang, T.Tang, C.Li, X.Liu, Z.Liu, B.Lei, C.Zhou. *Chemical Physics Letters*, 389, 176, 2004.

[36] G.Audoit, E.Mhuircheartaigh, S.Lipson, M.Morris, W.Blau, J. Holmes. *Journal of Material Chemistry*, 2005 (in press).

[37] J.Qi, A.Belcher, J.White. *Appllied Physics Letters*, 82, 2616, 2003.

[38] Y.Ahn, J.Dunning, J.Park. *Nano Letters*, 5, 1367, 2005.

[39] J.Kinaret, T.Nord, S.Viefers. Appllied Physics Letters, 82, 1287, 2003.

[40] M.Duquesnes, S.Rotkin, N.Aluru. *Nanotechnology* 13, 120, 2002.

[41] L.Jonsson, S.Axelsson, T.Nord, S.Viefers, J.Kinaret. Nanotechnology, 15, 1497, 2004.

[42] R.Boyd. Basic Medical Microbiology. *Little, Brown and Company*, Boston, 1991.

[43] C.Niemeyer. *Angewandte Chemie*, 113, 4254, 2001.

[44] C.A.Mirkin, R.L.Letsinger, R.C.Mucic, J.J.Storhoff. *Nature*, 382, 607, 1996.

[45] S.Connolly, D. Fitzmaurice. *Advanced Mater*ials, 11, 1202, 1999.

[46] W.Shenton, S.A. Davis, S.Mann. *Advanced Mater*ials, 11, 449, 1999.

[47] A.P.Alivisatos, K.Johnson, X.Peng, T.E.Wilson, C.J.Loweth, M.Bruchez, P.G.Schultz. *Nature*, 382, 609, 1996.

[48] N.C.Seeman. *Nature*, 421, 427, 2003.

[49] D.Porath, A.Bezryadin, S.deVries, C.Dekker. *Nature*, 400, 635, 2000.

[50] A.Rakitin, P.Aich, C.Papadopoulos, Y. Kobzar, A.Vedeneev, J.Lee, J.Xu. *Physical Review Letters,* 86, 3671, 2001.

[51] M.Maeda, Y.Mitsuhashihi, M. Takagi. *Analytical Sciences, 8*, 83, 1992.

[52] R.Wiesendanger. Scanning Probe Microscopy and Spectroscopy. *Cambrige University Press*, Cambrige, 1994.

[53] H.Olin. Scanning Probe Microscopy:Design and Applications. *PhD thesis*, Goteborg, 1993.

[54] K Lew, K. Redwing. *Journal of Crystal Growth*, *254*, 14, 2003.

[55] Y.Liang, C.Zhen, D. Zou, D. Xu. *Journal of American Chemical Society*, *126*, 16338, 2004.

[56] H.Masuda, K. Fukuda. *Science*, *268*, 1466, 1995.

[57] C.Kittel. Introduction to Solid State Physics. *John Wiley and Sons*, NewYork, 1978.

[58] T.Chiang, K.Frank, H.Freund, A.Goldmann, F.Himpsel et al. Landolt-Bornstein: Numerical Data and Functional Relationships in Science and Technology. *Springer*, 1989.

[59] G.Meng, A.Cao, J.-Y.Cheng, A.Vijayaraghavan, Y.Jung, M.Shima, P.Ajayan. *Journal of Appllied Physics*, *97*, 064303, 2005.

[60] S.Sze. Physics of semiconductor devices. *Wiley-Interscience,* New York, 1981.

[61] G.Gu, M.Burghard, G.Kim, G.Dusberg, P.Chiu, V. Krstic, W.Han. *Journal of Appllied Physics, 90*, 11, 2001.

[62] T.Hanrath, B. Korgel. *Journal of Physical Chemistry B*, *109*, 5518, 2005.

[63] R.Bube. Photoconductivity of Solids. *John Wiley and Sons*, NewYork, 1960.

[64] С.Рывкин. Фотоэлектрические процессы в полупроводниках. *Физматгиз*, Москва, 1963.

[65] H.Watakabe, T.Sameshima, H.Kanno, M.Miyao. *Thin Solid Flms*, in press.

[66] T.Moustakas, W.Paul. *Physical Review B*, 16, 14, 1564, 1977.

[67] R.Wagner, A.Levitt. Whisker Technology, *Wiley*, New York, 1970.

[68] Н.Беляев. Сопротивление материалов, *Наука*, Москва, 1976.

[69] Г.Кочегаров. *Письма в Журнал Технической Физики*, 25, 17, 29б 1999.
also at http://www.internationalcrystal.net/optics_10.htm

[70] Israelachvili. Intermolecular and surface forces. *Academic Press*, London, 1992.

[71] Г.И.Епифанов. Физика твёрдого тела. *Высшая школа*, Москва 1977.

[72] D.Wang,Y.-L.Chang, Q.Wang, J.Cao, D.Farmer, R.Gordon, H.Dai. *Journal of American Chemical Society*, 126, 11602, 2004.

[73] A.Cai, H.Zhang, H.Hua, Z,Zhang. Nanotechnology, 13, 627, 2002.

[74] K.Ziegler, B.Polyakov, J.Kulkarni, T.Crowley, K.Ryan, M.Morris, D. Erts, J.Holmes. *Journal of Material Chemistry*, 14, 4, 585, 2004.

[75] Steel A.B., Herne T.M., Tarlov M.J. (1998) *Analytical Chemistry,* 70, 4670-4677.

[76] Peterlinz K.A., Georgiadis R.M. *Journal of American Chemical Society,* 119, 3401, 1997.

[77] L.Olsson, N.Lin, V.Yakimov, R. Erlandsson. *Journal of Appllied Physics*, 84, 4060, 1998.

[78] K.Slowinski, R.Chamberlain, C.Miller, M.Majda. *Journal of American Chemical Society*, 119, 11 910, 1997.

[79] C. Mate, M. Lorentz, V.Novotny. *Journal of Chemical Phys*ics, 90, 7550, 1989.

[80] A.Dhinjwala, S. Granick. *Macromolecules*, 30, 1079, 1997.

[81] E.deSouza, R.Douglas, O.Tescheke. *Langmuir*, 13, 6012, 1997.

[82] X.Xia, M.Berkowitz. *Physical Review Letters,* 74, 3193, 1995.

[83] J.Simmons. *Journal of Applied Phys*ics, 34, 1793, 1963.

[84] J.Halbritten. *Appllied Physics A*, 68, 153, 1999.

[85] S.Joyce, R.Thomas, J.Houston, T.Michalske, R.Crooks. *Physical Review Lett*ers, 68, 2790, 1992.

[86] T.Kleine-Ostmann, C.Jordens, K.Baaske, T.Weimann, M.Hrabe, M.Koch. *Applied Phiscics Letters*, 88, 102102, 2006.

[87] N.Kovtyukhova, B.Martin, J.Mbindyo , T.Mallouk, M.Cabassi ,T.Mayer. *Materials Science and Engineering C*, 19, 255, 2002.

[88] G.Marsh. *Materials Today*, 38, February 2003.

[89] I.Willner, E.Katz. Bioelectronics. From Theory to Applications. *Wiley-VCH*, Weinheim, 2005.

ACKNOWLEDGMENTS

I would acknowledge all my teachers, colleagues, my friends and my family. In particular, I would thank very much my supervisor Dr. Donats Erts for teaching and training. It was him who introduced the experimental science to me. I acknowledge Dr. Yuris Prikulis, who never avoided to teach me many things. I would thank very much Dr. Emms Shidlovska, Dr. Girts Barinovs, Dr. Yuris Dzelme, Dr. Alexander Livshic and Dr. Boris Zapol for consulting me both in Physics and Philosophy. I would thank all my collegues from the Institute of Chemical Physics for help and friendship. I would pay my respect to Dr. Aleksey Katashev and Dr. Yurij Dehtjar for teaching me Physics and interesting discussions which expanded my erudition.

I would thank also:

Dr. Indrikis Muizhnieks and PhD student Uldis Malinovskis for participating in our DNA studies;

Dr. Larisa Grigorjeva and Dr. Donats Miller for great help in optical experiments on nanowire arrays;

Dr. Inta Muzikante and her students Andrey Tokmakov and Daiga Cepite for opportunity to participate in experiments on optically active molecular layers;

Dr. Maris Knite for possibility to participate in interesting studies on carbon black composite polymers;

Dr. Yuris Tiliks and Dr. Gunta Kizane as well as their group for help and collaboration;

Dr. Ants Lohmus and Dr. Rynno Lohmus as well as all their group from Institute of Physics of Tartu for numerous constructed apparatus and elegant technical solutions;

Dr. Justin Holmes and his group from Cork University-College (and particularly his brilliant PhD student Brian Daly) for producing the sample materials for my experiments on semiconducting nanowires;

Dr. Hakan Olin from Chalmers University for his great help in our research;

Dr. Eimer Tuite from Newcale University for great help in experiments on DNA arrays;

Dr. Bonifacas Vengalis and Dr. Vaclovas Lisauskas from Institute of Semiconducting Materials of Vilnius for help in nanowire arrays sample preparation for photoconductivity measurements;

I would acknowledge the University of Latvia, Latvian Academy of Sciences and European Social Fund for Scholarships and financial support.